Technical report; TR-207

KNMI

Retrieval of aerosol properties from multispectral direct sun measurements

O.P. Hasekamp

vrije Universiteit amsterdam

De Bilt, 1998

Koninklijk Nederlands Meteorologisch Instituut

Technical report = technisch rapport; TR - 207

De Bilt, 1997

PO Box 201
3730 AE De Bilt
Wilhelminalaan 10
De Bilt
The Netherlands
Telephone + 31(0)30-220 69 11
Telefax + 31 (0)30-221 04 07

Author: O.P. Hasekamp

UDC: 551.501.71
551.501.721
551.501.793

ISSN: 0169-1708

ISBN: 90-369-2142-2

● ● ● ●

Retrieval of aerosol properties from multispectral direct sun measurements

O.P. Hasekamp

Graduation Report Astronomy Group, Free University, Amsterdam

Supervisor at KNMI: Piet Stammes

May, 1998

Voorwoord

Dit verslag beschrijft het werk dat ik op het KNMI gedaan heb als afstudeeropdracht vanuit de Sterrenkunde groep van de Vrije Universiteit te Amsterdam. Een aantal mensen die mij bij dit werk gesteund hebben wil ik hier bedanken. In de eerste plaats mijn begeleider Piet Stammes. Van zijn begeleiding bij het werk en zijn commentaar op het verslag heb ik veel geleerd. Ook wil ik Robert Koelemeijer bedanken voor de onmisbare hulp bij het programmeren. Natuurlijk gaat mijn dank eveneens uit naar iedereen van de Wolken en Straling groep op het KNMI voor de gezellige tijd die ik daar gehad heb. Van de Sterrenkunde groep van de VU ben ik Johan de Haan en Professor Hovenier dankbaar voor de tijd die zij aan mijn verslag besteed hebben.

Voor de morele steun wil ik mijn moeder, zus, vader en vrienden bedanken en natuurlijk Edith die altijd geinteresseerd was in mijn werk en me erg gestimuleerd heeft.

Otto Hasekamp, 26 mei 1998

Contents

Abstract

From measurements, made with a new sunphotometer, the multispectral aerosol optical thickness has been derived. This has been done by using the Langley method. An algorithm has been developped for the automatic removal of data points taken during unstable atmospheric conditions. This method worked well for measurements taken in De Bilt. At 26 mornings and afternoons between July and November 1997 the aerosol optical thickness has been determined. The aerosol optical thickness appeared most of the time to be higher in summer than in autumn. To derive the aerosol optical thickness for unstable atmospheric conditions, an accurate calibration of the sunphotometer is needed. This can be done by the Langley method but more Langley plots are needed for this than are available now.

From the multispectral measurements of the aerosol optical thickness the aerosol size distribution has been retrieved using a constrained linear inversion method. The inversion algorithm was first applied to simulated data of the aerosol optical thickness to find optimal settings for parameters used in the inversion and to obtain insight in the accuracy of the inversion algorithm. Because from the sunphotometer measurements the aerosol size distribution can only be retrieved in a limited radius range, the retrieved size distributions are extrapolated to smaller radii with a Junge power law.

Time series of the effective radius and effective variance of the aerosol size distributions, retrieved from real measurements, are presented as well as some representative size distributions. In summer the effective radius appeared to be smaller and the effective variance appeared to be larger than in autumn.

1 Introduction

Aerosols are small solid or liquid particles that are found in all planetary atmospheres. For many reasons knowledge about aerosols is important. One of these reasons is the climate impact of aerosols. They influence the Earth's radiation budget by scattering and absorption in the visable part of the spectrum and by absorption-emission in the infrared (Lenoble, 1984). The resulting effect (warming or cooling) strongly depends on the particle characteristics. Besides their direct influence on radiation, aerosols also have an indirect influence, because they play an important role in the formation of clouds, by permitting the condensation of water vapour into cloud droplets or crystals. Generally the effect of increasing the aerosol amount is an increase of the planetary reflectance, i.e., a cooling of the surface-atmosphere system. The way in which this cooling can counteract the greenhouse warming of CO_2 and other trace gases has been studied e.g. by Hansen and Lacis (1990). Another reason why knowledge about aerosols is important, is that they induce disturbances in remote sensing measurements of other atmospheric constituents and of the surface.

Because the influences, mentioned above, depend on several properties of aerosols, it is necessary to obtain information about such properties at different geographical locations during a long period. Two important aerosol parameters are: the spectral dependency of the aerosol optical thickness and the aerosol size distribution. The multispectral aerosol optical thickness of the atmosphere can be derived from direct sun measurements with a sunphotometer. In this study the first measurements are made with a new sunphotometer at the KNMI in De Bilt. This sunphotometer is called the SPUV (Sun Photometer UV). From the spectral dependency of the aerosol optical thickness, the aerosol size distribution can be retrieved. This is an inverse radiative transfer problem. Inverse problems often occur in remote sensing and are the subject of active mathematical research. In remote sensing a few popular ways to solve inverse problems are: the optical estimation theory (Rodgers, 1976, 1990), relaxation methods (Chahine, 1972, Chu, 1985) and the constrained linear inverse technique (e.g. Twomey, 1977, King et al. , 1978). In this study the main steps of the variant of King et al. (1978) of the constrained linear inversion method are used.

In Section 2 of this report the derivation of the aerosol optical thickness from the direct sun measurements by means of the Langley method is explained. For this method in principle clear sky conditions are required. However, in the Netherlands these conditions are often violated by clouds. Therefore, the greatest part of this chapter is dedicated to solving the problem of cloudy sky conditions.

The method of inversion of the optical thickness measurements to infer the aerosol size distribution is described in Section 3, including the problems that occur in this inversion and their solutions.

Before the inversion algorithm was applied to real data it was applied to optical thickness data which were simulated using known size distributions, to get insight in the reliability of the inverted size distribution and to find the optimal settings for parameters used in the inversion. This is described in Section 4.

Section 5 describes the experimental setup of the SPUV. Various problems were encountered when doing the first measurements with the new instrument. These problems are evaluated in this chapter.

Results of the SPUV measurements done at the KNMI are shown in Section 6 and furthermore their accuracy is discussed. Also a few size distributions are shown which are derived from these measurements and time series are given of the effective radius and the effective variance of the retrieved distributions.

The conclusions and recommendations for further research are given in Section 7.

2 Sunphotometry

2.1 Lambert-Beer's law

The solar irradiance that reaches the Earth's surface has been attenuated along its path in the atmosphere due to scattering and absorption by molecules and aerosols.

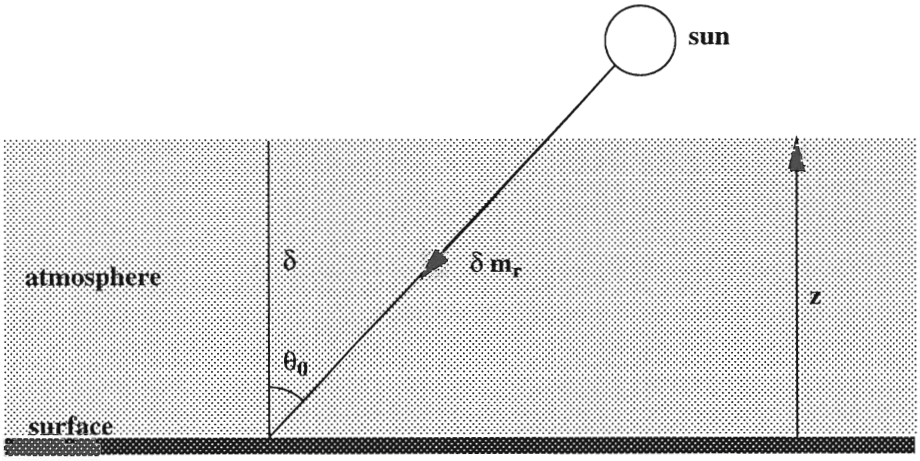

Figure 1: *Plane parallel atmosphere.*

The irradiance I of the direct solar radiation at a certain wavelength λ that is measured perpendicular to the Sun at the Earth's surface is given by Lambert-Beer's law:

$$I(\lambda) = I_0(\lambda)\mathrm{e}^{-l(\lambda)}, \tag{1}$$

where $I_0(\lambda)$ is the incoming solar irradiance at the top of the Earths atmosphere and $l(\lambda)$ is the slant optical path length of the radiation through the atmosphere, which is defined by:

$$l(\lambda) = \int_0^\infty k\rho ds, \tag{2}$$

where $k(\lambda)$ ($\mathrm{m}^2.\mathrm{kg}^{-1}$) is the mass extinction coefficient and $\rho(z)$ ($\mathrm{kg.m}^{-3}$) is the local density. The integration over s is over the slant path through the atmosphere. The optical thickness, $\delta(\lambda)$, of the atmosphere is defined by:

$$\delta(\lambda) = \int_0^\infty k\rho dz, \tag{3}$$

where the integration over z is over the vertical direction of the atmosphere. The relative airmass factor, m_r, converts $\delta(\lambda)$ in $l(\lambda)$:

$$l(\lambda) = \delta(\lambda)m_r. \tag{4}$$

From Eq. (2), (3) and (4) it follows that m_r is defined by:

$$m_r = \frac{\int_0^\infty \rho ds}{\int_0^\infty \rho dz} \tag{5}$$

If the curvature of the Earth's atmosphere and refraction are neglected, it follows from Fig. 1 that the airmass factor is given by:

$$m_r = \frac{1}{\cos\theta_0}. \tag{6}$$

Here θ_0 is the solar zenith angle. For values of $\theta_0 < 60^o$ the error made when using Eq. (6) is less then 0.1 % (Wauben, 1996). When taking into account the sphericity of and refraction in the atmosphere the vertical distribution of the different attenuating substances are required in order to calculate m_r from Eq. (5) for each substance. The general expression for the relative airmass between altitudes z_0 and z_1 of an atmospheric constituent with density n at altitude z for a spherical atmosphere including refraction may be written as (McClatchey, 1972, pp. 40-42)

$$m_r = \left[\int_{z_0}^{z_1} n(z)dz\right]^{-1} \int_{z_0}^{z_1} \left[1 - \left(\frac{R+z_0}{R+z}\right)^2 \left(\frac{m(z_0)}{m(z)}\cos\gamma\right)^2\right]^{-1/2} n(z)dz, \tag{7}$$

where m is the refractive index of air, R is the radius of the earth and γ is given by: $\gamma = 90^o - \theta_0$. Results of calculations with Eq. 7 can be used to obtain approximative expressions for m_r. In this way Kasten (1966) made the following approximation for m_r for scattering by molecules taking into account the curvature of and refraction in the atmosphere:

$$m_r = \frac{1}{sin\gamma + a(\gamma + b)^c}, \tag{8}$$

where a, b and c are constants. According to Kasten and Young (1989): a=0.050572, b=6.007995^o and c=1.6264. This approximation is used in this study. However, gas absorption and scattering by aerosols are not taken into account in Eq. (8). This leads to an error in m_r in Eq. (8) of less than 1% for values of $\theta_0 < 85^o$ (Wauben, 1996).

The optical thickness of the atmosphere can be written as

$$\delta(\lambda) = \delta_R(\lambda) + \delta_g(\lambda) + \delta_a(\lambda), \tag{9}$$

where $\delta_R(\lambda)$ is the optical thickness due to Rayleigh scattering, $\delta_g(\lambda)$ is the optical thickness due to gas absorption and $\delta_a(\lambda)$ is the optical thickness due to scattering and absorption by aerosols, called the aerosol optical thickness.

2.2 Langley method

The Langley method uses the daily motion of the sun along the sky to determine the aerosol optical thickness of the atmosphere. Since the solar zenith angle changes during the day, the relative airmass factor changes. Writing Eq. (1) as

$$\ln I(\lambda) = \ln I_0(\lambda) - \delta(\lambda)m_r, \tag{10}$$

it is easy to see that there is a linear dependency between $\ln I(\lambda)$ and m_r, when a constant optical thickness may be assumed during a certain period of a day. So when $I(\lambda)$ is measured at different times during a day (so for different values of m_r), a plot can be made of $\ln I(\lambda)$ versus m_r. Such a plot is called a Langley plot. From such a plot the optical thickness $\delta(\lambda)$ of the atmosphere can be determined because it is the slope of the linear regression fit of $\ln I(\lambda)$ versus m_r. If $I(\lambda)$ is measured outside molecular absorption lines or at wavelengths where $\delta_g(\lambda)$ is known, the aerosol optical thickness $\delta_a(\lambda)$ can be determined from the total optical thickness $\delta(\lambda)$ with Eq. (9), because the Rayleigh optical thickness is a known function of wavelength and ground pressure.

The important condition of a constant optical thickness during the period of the Langley plot is often violated because of cloud passages. These cloud passages produce dips in the Langley plot, so datapoints taken during cloud passages have to be removed from the data set. The remaining datapoints can be used for a least-squares regression to obtain the aerosol optical thickness. The method used for 'removal' of cloud passages is described in Sect. 2.2.2. On days during which $\delta_a(\lambda)$ is variable with time, the Langley method cannot be used.

2.2.1 Calibration by the Langley method

When using the Langley method for determining the optical thickness, it is not necessary to use a calibrated sunphotometer, because the slope of the Langley plot is independent of the calibration of the instrument. On the other hand, the Langley method can be used to calibrate the sunphotometer. This can be done by extrapolating the regression line to zero airmass . The intercept with the $\ln I(\lambda)$-axis should give the extra terrestrial solar irradiance, $I_0(\lambda)$, which is a known quantity. Comparing the intercept of the Langley plot with the value $\ln I_0(\lambda)$, found from tabulated values of $I_0(\lambda)$, gives the calibration constant of the sunphotometer.

A necessary condition for the Langley method, however, is the stability of the sunphotometer. The value found for $\ln I_0(\lambda)$ can be used to check this stability, since this value may not change from day to day, apart from the changing distance between Sun and Earth.

The advantage of using a calibrated sunphotometer is that the variation of the aerosol optical thickness during the day can be measured. To find the optical thickness at a certain time of the day, only one instantaneous absolute measurement of $I(\lambda)$ is needed. The optical thickness at a certain time t of the day is then given by:

$$\delta(\lambda, t) = \frac{\ln I_0(\lambda, t) - \ln I(\lambda)}{m_r(t)}. \tag{11}$$

This method can be used at each time the direct solar irradiance can be measured. The condition of a constant optical thickness during a certain period of a day is then no longer needed. However, also for calibrated measurements of $I(\lambda)$, it is still useful to apply Langley analysis to check the stability of the sunphotometer.

2.2.2 Removal of cloud passages

Harrison and Michalsky (1994) have published an algorithm for automatic analysis of sunphotometer data including a method for removing data points taken during cloud passages. This algorithm consists of a sequence of "filters" that reject useless points. The five filters are:

1. The airmass range is restricted to airmasses between 2 and 6 (this corresponds to solar zenith angles of 60^o and 80^o). This airmass range is covered in a relatively short time, so one can assume a constant optical thickness during this period, which is an important condition for Langley analysis. Airmasses higher than 6 are not used, because for those airmasses uncertainty exists about the refraction correction for the airmass.

2. In Eq. (10) can be seen that a constant aerosol optical thickness results in a Langley plot with a negative slope. Harrison and Michalsky (1994) assume that cloud passages produce minima in the Langley plot followed by a period where the Langley plot has a positive slope. Therefore, this filter identifies regions where the slope $\frac{dI}{dm_r}$ is positive and rejects these points. The number of points corresponding to the cloud passage left of the minimum in the Langley plot is assumed to be equal to the points with positive slope, right of the minimum. The second filter also reject these points.

3. Points where the slope $\frac{dI}{dm_r}$ is more than twice its mean are also rejected. These points correspond to cloud passages near the edge of the selected airmass range and points where filter (2) is not agressive enough.

4. The remaining points are used for a least-squares regression. The points that lie more than 1.5 σ (standard deviation) from the regression line are rejected.

5. The remaining points are used for the final Langley plot. The Langley analysis is assumed to be valid only when 1/3 of the initial points remain after filtering and $\sigma < 0.006$.

Harrison and Michalsky (1994) state that it is a well working algorithm, even for difficult sites (sites with many cloud passages). However, for a few days, data taken in De Bilt were analyzed with this algorithm with an unsatisfactory result. An example of analysis in this way is shown in Fig. (2).

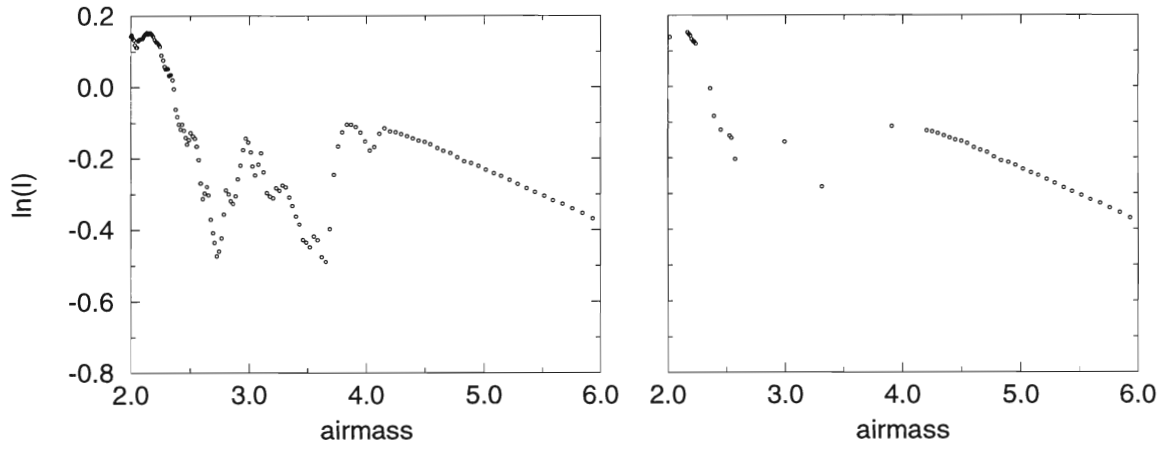

Figure 2: *Example of data analysis with the algorithm of Harrison and Michalsky (1994). The figure on the left contains all the data points, the figure on the right contains the datapoints that remain after 'filtering' with the algorithm. Morning Langley plot of August 12th, 1997.* $\lambda = 670nm$

This figure shows a morning Langley plot in which the points between airmass 4 and 6 are useful for Langley analysis and the datapoints between airmass 2 and 4 correspond to a cloud passage. It is easy to see that the data points that remain after filtering with the algorithm (on the right in Fig. 2) are not all useful for linear regression. For other days similar problems appeared. It was found that the algorithm only works for almost clear days with only a few little dips in the Langley plot, like the dip near airmass 4 in Fig. (2). It is obvious that this way of data analysis is not useful for a site like De Bilt. The reason for this becomes clear when considering the second filter in the algorithm of Harrison and Michalsky. This filter assumes that cloud passages produce smooth dips in the Langley plot and the algorithm only works well for these kind of dips. In reality, clouds more often produce large dips like in Fig. 2. The filter does not work for this kind of cloud passages because "inside" the cloud passage the slope becomes negative and positive more than once. Therefore a more agressive method is needed for removal of cloud passages that are typical for De Bilt. The method used in this study is as follows:

1.
   - Determine the first point of a cloud passage: $m_r = m_r^*$ and $I = I^*$
   - From this first point, remove all points (m_r,I) for which $\frac{\ln I^* - \ln I}{m_r^* - m_r} > 0$. Most of the points of the cloud passages are removed now.

2.
   - Make an estimate δ_{est} of the optical thickness, using only the points points for which $-0.05 < \frac{d^2}{dm_r{}^2} \ln I < 0.05$. These are points for which δ does not vary much in time.

- Remove all points for which $|\frac{dI}{dm_r}| > |0.5\delta_{est}|$. These are cloud passage points that remained after step 1 and cloud passages near the edge of the airmass range. It is decided to choose the value $0.5\delta_{est}$ after evaluating the influence of this value for data of different days.

3. The third step is the same as filter 4 in the algorithm of Harrison and Michalsky, i.e. removing all the points that lie more than 1.5 σ from the regression line.

In the present data analysis an airmass range is chosen between 2 and 6, as suggested by Harrison and Michalsky (1994). This is decided after having evaluated the effect of longer airmass ranges. The chosen airmass range appeared to be one where one could assume a constant aerosol optical thickness. In figure 3 it is shown how this new filtering process works for the same data as in figure 2.

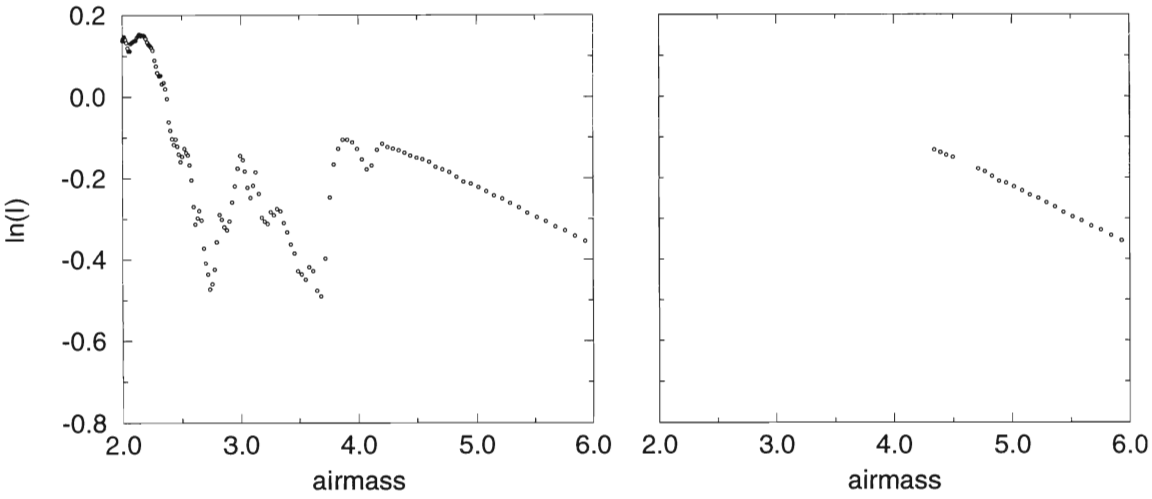

Figure 3: *Example of data analysis in the new way. The figure on the left contains all the datapoints, the figure on the right contains the datapoints that remain after 'filtering' with the new algorithm. Morning Langley plot of August 12th, 1997.* $\lambda = 670nm$

Clearly, for this day the new method for removing clouds works better than the algorithm of Harrison and Michalsky. Also for other days the new method gave satisfactory results. So, for the data analysis in this study, the new method is used.

All days for which more than 5% of the datapoints remained after filtering were used to determine the aerosol optical thickness. An indication of the reliability of the determined $\delta(\lambda)$ is is of course given by the standard deviation of the regression fit. Another check of reliability of the determined δ is the value found for $\ln I_0(\lambda)$ by the Langley method. Days for which this value deviates too much from the average value found for $\ln I_0(\lambda)$ should not be used to determine the optical thickness by the Langley method.

3 Procedure for retrieving aerosol size distributions

3.1 Ångström's turbidity law

Ångström (1930) found the following empirical relation for the spectral dependency of the aerosol optical thickness. This relation is:

$$\delta(\lambda) = \beta\lambda^{-\alpha}, \tag{12}$$

in which α and β are called the Ångström turbidity parameters. α gives an indication of the size of the aerosols and has typical values between 0.5 and 2.5. A small value of α indicates that there are many large aerosols in the atmosphere and a large value of α indicates that there are many small aerosols. β is related to the total number of aerosols in the atmosphere.

3.2 Size distribution of aerosols

The aerosol size distribution is variable with time and depends on the geographical location. In this study the aerosol size distribution, $n(r)$, is defined as the number of aerosols per unit area per unit radius interval in a vertical column of the atmosphere. Often the real size distribution is not known and for many purposes (e.g. radiative transfer models, satellite aerosol retrieval) standard aerosol models are used. The size distribution is then represented by a mathematical expression with a few adjustable parameters. An important parameter for the aerosol size distribution is the effective radius, introduced by Hansen and Travis (1974):

$$r_{eff} = \frac{\int_0^\infty r\pi r^2 n(r)dr}{\int_0^\infty \pi r^2 n(r)dr} = \frac{1}{G}\int_0^\infty r\pi r^2 n(r)dr. \tag{13}$$

r_{eff} is a measure for the optically mean radius of the distribution. The associated effective variance is (Hansen and Travis, 1974):

$$v_{eff} = \frac{1}{G r_{eff}^2}\int_0^\infty (r - r_{eff})^2 \pi r^2 n(r)dr. \tag{14}$$

v_{eff} is a measure for the width of the distribution. The two parameters r_{eff} and v_{eff} are useful, because two size distributions that are different but have the same r_{eff} and v_{eff} lead to similar radiative characteristics of the aerosol.

The most popular distributions are (Lenoble 1993, Hansen and Travis 1974):

Junge power law
Between radii r_1 and r_2, the Junge power law is defined as:

$$n(r) = Cr^{-\nu-1} \tag{15}$$

and $n(r) = 0$ for other values of r. In Eq. (15), ν is given by $\nu = \alpha + 2$ where α is one of the Ångström turbidity parameters. The constant C is fixed by the total number of particles.

Log-normal distribution:

$$n(r) = C\frac{1}{r}\exp[-(\ln r - \ln r_g)^2/(2\sigma)^2]. \tag{16}$$

Here σ is given by: $\log\sigma = \sqrt{\log(1 + v_{eff})}$ and r_g is given by: $r_g = r_{eff}/(1 + v_{eff})^{2.5}$. C depends on the total number of particles and σ.

Two-parameter gamma distribution:

$$n(r) = Cr^{(1-3b)/b} \exp(-r/ab). \tag{17}$$

Here: $a = r_{eff}$ and $b = v_{eff}$.

3.3 Inversion equation

From measurements of the aerosol optical thickness at different wavelengths, $\delta_a(\lambda)$, the aerosol size distribution can be obtained. If all aerosols in the atmosphere are assumed to be spherical and an homogeneous aerosol distribution in the atmosphere may be assumed, the spectral dependence of the aerosol optical thickness can be written as:

$$\delta_a(\lambda) = \int_0^\infty \pi r^2 Q_e(r, \lambda, m) n(r) dr, \tag{18}$$

where is Q_e the extinction efficiency factor , calculated by using Mie scattering theory for spherical particles (Van de Hulst (1957)) and m is the complex refractive index which is considered to be independent of height. To obtain the size distribution from Eq. (18), finite boundaries (r_a and r_b) of integration have to be chosen and the integral in Eq. (18) has to be written as a finite sum over small radius intervals. For each wavelength λ_i for which measurements of $\delta_a(\lambda)$ are available, we may write:

$$\delta_a(\lambda_i) = \int_{r_a}^{r_b} \pi r^2 Q_e(r, \lambda_i, m) n(r) dr = \sum_{j=1}^{N} \int_{r_j}^{r_{j+1}} \pi r^2 Q_e(r, \lambda_i, m) n(r) dr. \tag{19}$$

Assuming that $n(r)$ is constant over each interval $[r_j, r_{j+1}]$, Eq. (19)can be written in matrix form as:

$$\mathbf{g} = \mathbf{A}\mathbf{f} + \mathbf{e}. \tag{20}$$

In this equation $\mathbf{g}$ is a vector of dimension M, of which each element g_i represents the measured values of the optical thickness at λ_i: $\delta_a(\lambda_i)$.
$\mathbf{f}$ is a vector of dimension N which represents $n(r)$. The element f_j represents the value of $n(r)$ at the midvalue of the radius interval $[r_j, r_{j+1}]$.
$\mathbf{A}$ is a $M \times N$ matrix, which is called the kernel matrix. Each element of $\mathbf{A}$ can be written as:

$$A_{ij} = \int_{r_j}^{r_{j+1}} \pi r^2 Q_e(r, \lambda_i, m) dr. \tag{21}$$

In Eq. (20) $\mathbf{e}$ is an unknown error vector of M elements e_i which are given by:

$$e_i = g_i - \sum_j A_{ij} f_j. \tag{22}$$

The vector $\mathbf{e}$ represents the deviation between measurements and model.

3.4 Problems involved with inversion

As described e.g. by Twomey (1977) the inversion of Eq. (20) is not at all straightforward. On first sight, it seems obvious to use the standard method for solving a set of M linear equations in M unknowns, namely:

$$\mathbf{f} = \mathbf{A}^{-1}\mathbf{g}. \tag{23}$$

However, this leads to a very unstable solution for $\mathbf{f}$. This is a result of interdependence among the rows of $\mathbf{A}$, i.e. some of the rows of $\mathbf{A}$ can be expressed by a linear combination of other rows. So, in fact less than M linear equations are available. Doing measurements of $\delta_a(\lambda)$ at more wavelengths will not improve the retrieval because more rows in $\mathbf{A}$ would lead to a higher interdependency among the rows of $\mathbf{A}$. Apparently, the multispectral measurements of $\delta_a(\lambda)$ do not contain sufficient information about $n(r)$. This means that $n(r)$ is not uniquely defined by the different measurements $\delta_a(\lambda_i)$, i.e., a set of different solution vectors $\mathbf{f}$ exist.

To obtain a solution for $\mathbf{f}$, two possibilities exist. One is to add information to the system of linear equations in Eq. (19), external to the measurements. Another possibility is to impose a constraint on the solution. With this constraint one $\mathbf{f}$ can be chosen among the set of solution vectors. Many methods have been proposed for solving inversion problems. A popular method is the optimal estimation method (Rodgers 1976), which relies on previous knowledge of the solution, based for example on climatological data. However, because the aerosol size distribution is known to be very time dependent, this method is not useful for the retrieval of this quantity.

3.5 Constrained linear inversion method

Among the various methods for dealing with inverse problems, that have been proposed during the past years, the constrained linear inversion method of King et al. (1978) is one of the most popular methods for retrieval of the aerosol size distribution. For recent applications of this method see for example Herman et al. (1997) and Gonzalez and Ogren (1996). In the constrained linear inversion algorithm three constraints are imposed on the solution $\mathbf{f}$, namely:

- A smoothing constraint, i.e. the smoothest of the possible solutions is chosen
- $\sum_i {e_i}^2$ is minimized
- All elements of $\mathbf{f}$ must be positive

The form of $n(r)$ is being partially assumed. In this way information is added to Eq. (19). The added information and constraints are discussed below.

3.5.1 Assumptions regarding the form of the size distribution

In the constrained linear inversion method of King et al. (1978), the form of $n(r)$ is being partially assumed by writing:

$$n(r) = f(r)h(r), \tag{24}$$

where $h(r)$ is the Junge power law (Eq. (15)) which is a rapidly varying function with r and $f(r)$ is a slowly varying function with r. Because information about $n(r)$ is added to the inversion algorithm it is no longer necessary that the number of inverted sizes (i.e. the number of unknowns in Eq. (20)) equals the number of wavelengths at which measurements of $\delta_a(\lambda)$ are available. $\mathbf{f}$ now is a vector of dimension N and $\mathbf{A}$ is a $M \times N$ matrix with $N \geq M$. The set of linear equations in Eq. (19) can now be written as:

$$\delta_a(\lambda_i) = \sum_{j=1}^{N} f(r) \int_{r_j}^{r_{j+1}} \pi r^2 Q_e(r, \lambda_i, m) h(r) dr. \tag{25}$$

In this way the quadrature error is reduced because the assumption of a constant $f(r)$ for each interval $[r_j, r_{j+1}]$ is more plausible than it was for $n(r)$, because $f(r)$ is more slowly varying with r. For each

element of **A** can now be written:

$$A_{ij} = \int_{r_j}^{r_{j+1}} Q_e(r, \lambda_i, m) h(r) dr. \tag{26}$$

The solution vector **f** now represents the function $f(r)$ in Eq. (24).

3.5.2 Constraints on the solution

For the smoothing constraint, which is imposed on the solution, the measure of smoothness is used that is proposed by Phillips (1962). He states that the smoothest solution, is the solution for which the sum of the squares of the second derivatives of the solution points is minimized. The condition of choosing the smoothest $f(r)$ is combined with the constraint that $\sum_i {e_i}^2$ is minimized. Taking into account these two constraints, the procedure consists of minimizing the performance function Q (Phillips, 1962):

$$Q = Q_1 + \gamma Q_2, \tag{27}$$

where γ is a non negative Lagrange multiplier. Since at the minimum of a function the first derivative equals zero, Q is differentiated with respect to each of the N elements f_k of **f**, in order to find the minimum of Q. This results in a set of N equations:

$$\frac{d}{df_k} Q = \frac{d}{df_k} Q_1 + \gamma \frac{d}{df_k} Q_2 = 0. \tag{28}$$

Q_1 is given by:

$$Q_1 = \sum_{i=1}^{M} {e_i}^2. \tag{29}$$

Often some information is available about **e** in the form of measurement errors in $\delta(\lambda_i)$. Q_1 can now be written as:

$$Q_1 = \sum_{i=1}^{M} \sum_{j=1}^{M} C_{ij}^{-1} e_i e_j. \tag{30}$$

Here C_{ij} is an element of the measurement covariance matrix **C**, from which the diagonal elements are given by the measurement errors in the $\delta_a(\lambda)$ and the other elements are given by the correlations between these measurement errors (see e.g. Liebelt 1967). In most cases, the measurement errors are uncorrelated and **C** is a diagonal matrix. Using Eq. (22) for the e_i results in:

$$Q_1 = -\sum_{i=1}^{M} \sum_{j=1}^{M} \sum_{k=1}^{N} C_{ij}^{-1} (A_{ik} f_k - g_i) e_j. \tag{31}$$

Differentiating Q_1 with respect to f_k gives:

$$\frac{d}{df_k} Q_1 = -\sum_{i=1}^{M} \sum_{j=1}^{M} C_{ij}^{-1} A_{ik} e_j. \tag{32}$$

Q_2 represents the measure of smoothness (Phillips, 1962):

$$Q_2 = \int_{r_1}^{r_N} (f(r))^2 dr, \tag{33}$$

where $f(r)$ is taken from Eq. (24). When the derivative of $f(r)$ in each point r_j is approximated by $f'(r) = \frac{f(r_j)-f(r_{j-1})}{r_j-r_{j-1}}$, Eq. (33) can be expressed in the elements f_k of $\mathbf{f}$:

$$Q_2 = \sum_{k=2}^{N-1} (f_{k-1} - 2f_k + f_{k+1})^2. \tag{34}$$

Twomey (1977) composed a matrix $\mathbf{H}$, called a smoothing matrix, such that Eq. (34) can be written as:

$$Q_2 = \sum_{k=1}^{N} \sum_{j=1}^{N} f_k H_{kj} f_j. \tag{35}$$

Here H_{kj} is an element of $\mathbf{H}$. Differentiating Q_2 with respect to f_k gives:

$$\frac{d}{df_k} Q_2 = \sum_{j=1}^{N} H_{kj} f_j. \tag{36}$$

With the expressions obtained for $\frac{d}{df_k}Q_1$ and $\frac{d}{df_k}Q_2$ the N equations in Eq. (28) can be written as:

$$-\sum_{i=1}^{M} \sum_{j=1}^{M} C_{ij}^{-1} A_{ik} e_j + \gamma \sum_{j=1}^{N} H_{k,j} f_j = 0. \tag{37}$$

In matrix form this can be written as:

$$-\mathbf{A}^T\mathbf{C}^{-1}\mathbf{e} + \gamma\mathbf{H}\mathbf{f} = 0. \tag{38}$$

Combining Eq. (38) with the original problem (Eq. (20)), and eliminating $\mathbf{e}$, leads to the solution for $\mathbf{f}$:

$$\mathbf{f} = \left(\mathbf{A}^T\mathbf{C}^{-1}\mathbf{A} + \gamma\mathbf{H}\right)^{-1}\mathbf{A}^T\mathbf{C}^{-1}\mathbf{g}. \tag{39}$$

In this equation the value of γ is related to the influence of the smoothing constraint. A suitable value for γ is found, taking into account the constraint that all elements of $\mathbf{f}$ must be positive. Since γ enters Eq. (39) in a manner such that the elements of the matrix $\gamma\mathbf{H}$ are to be added to the elements of $\mathbf{A^T C^{-1} A}$ to produce the desired smoothing, the magnitudes of the $\gamma H_{ij}/(A^T C^{-1} A)_{ij}$ are of importance. Therefore, a relative gamma is introduced by King et al. (1977), defined as:

$$\gamma_{rel} = \frac{\gamma H_{11}}{(A^T C^{-1} A)_{11}}. \tag{40}$$

If γ_{rel} becomes very small (approaching to zero) the constrained linear inversion equation (Eq. (39)) reduces to that of direct inversion (Eq. (23)), which leads to unstable solutions. If, on the other hand, γ_{rel} becomes very large, the solution is constrained too much. This means that the smoothing constraint influences the solution much more than the measurements and the kernel matrix. Both effects (too small or too large γ_{rel}) are undesirable. King (1982) suggested that the best γ is found by varying γ_{rel} between 10^{-3} and 1, and to choose the smallest value of γ_{rel} for which all elements of $\mathbf{f}$ are positive.

3.5.3 Iterative procedure

With Eq. (39) the aerosol size distribution can be obtained. This is done by an iterative procedure. The first iteration consists of applying the constrained linear inversion as described above. This results

in a size distribution: $n^{(1)}(r) = f^{(1)}(r)h(r)$ (see Eq. (24)). The second iteration consists of the same procedure as the first iteration with the only difference that $n^{(1)}(r)$ takes in the place of $h(r)$. This results in a size distribution: $n^{(2)}(r) = f^{(2)}(r)n^{(1)}(r)$ which is used for the third iteration. The iteration continues until a stable solution is reached. This is after a iteration (j) when $n^{(j)}(r) = n^{(j-1)}(r)$ within 1%. For each iteration $j > 1$ the elements of $\mathbf{A}^{(j)}$ are given by:

$$A_{ij}^{(j)} = \int_{r_j}^{r_{j+1}} \pi r^2 Q_e(r, \lambda_i, m) n^{(j-1)}(r) dr. \tag{41}$$

4 Tests of the retrieval procedure using simulated data

4.1 Introduction

The inversion method was first applied to simulated data of the aerosol optical thickness. This is useful for two purposes:

- To find the influence on the retrieval of several parameter choices, like the radius interval of the retrieval, the number of inverted sizes, the value of the Lagrange multiplier γ and the number of wavelengths at which measurements of $\delta_a(\lambda)$ are available.
- To obtain insight in the accuracy of the retrieval procedure.

4.2 Aspects of Mie calculations

For the simulation, the aerosol optical thickness was calculated according to Mie theory for standard size distributions. The size distribution retrieved from these simulated data was compared to the original size distribution. Also the values of r_{eff} and v_{eff} were compared to those of the original size distribution. The standard distributions used for simulation of optical thickness data were log -normal and two-parameter gamma distributions with various values for r_{eff} and v_{eff}.

The wavelengths chosen for the Mie calculations were: 368 nm, 500 nm, 670 nm, 780 nm and 870 nm. These are wavelengths at which measurements are made with the available sunphotometer. The refractive index used for the Mie calculations is $1.53 - 0.005i$ for all wavelengths. This is the refractive index for water soluble aerosols taken from a Standard Radiation Atmosphere (Radiation Commission of IAMAP (1986)). The Mie calculations (for the simulations and for the calculation of the elements of $\mathbf{A}$) were performed using subroutines of the Meerhoff Mie program (De Rooij and Van der Stap, 1983). The inverse of the matrix $\mathbf{A}^T\mathbf{C}^{-1}\mathbf{A} + \gamma\mathbf{H}$ (Eq. (39)) cannot be calculated in a straightforward way, because in some cases this matrix is close to singular. Therefore, singular value decomposition (Press et al., 1986) was used for calculating inverse matrices. This worked well in all cases.

4.3 Optimal choice of parameters

4.3.1 A limited radius range

The aerosol size distribution can only be retrieved in a certain radius range r_{min} to r_{max} (e.g. Heintzenberg et al., 1981). This can be understood by looking at the elements of the kernel matrix (Eq. (26)) plotted against radius in Fig. (4) for $\lambda = 368$ nm and $\lambda = 870$ nm (i.e. the minimum and maximum wavelengths for which measurements of $\delta_a(\lambda)$ were made in this study). For the exponent ν in the power law $h(r)$ a value of 3.8 is taken in this figure (corresponding to a turbidity coefficient α of 1.8, which often occurs in practice). The kernel elements for the other wavelengths lie between these two lines. In Fig. 4 can clearly be seen that the linear dependence between the two kernels becomes higher with increasing r. If r exceeds a certain value r_{max} the kernels are totally linear dependent. The matrix $\mathbf{A}$ clearly contains no information about the size of the particles when $r > r_{max}$. If $r < r_{min}$ the elements of $\mathbf{A}$ become too small and $\mathbf{A}$ contains no information about the particle size. Obviously the retrieval is most accurate in the radius range where the different kernels are mostly linear independent.

Applying the inversion to the simulated data, it became clear that in most cases problems occured with the inversion for radii lower than 0.1μm. For these low radii often negative (so aphysical) solutions were found for the size distribution. When r_{max} exceeded the value of 0.8 μm the result of the retrieval

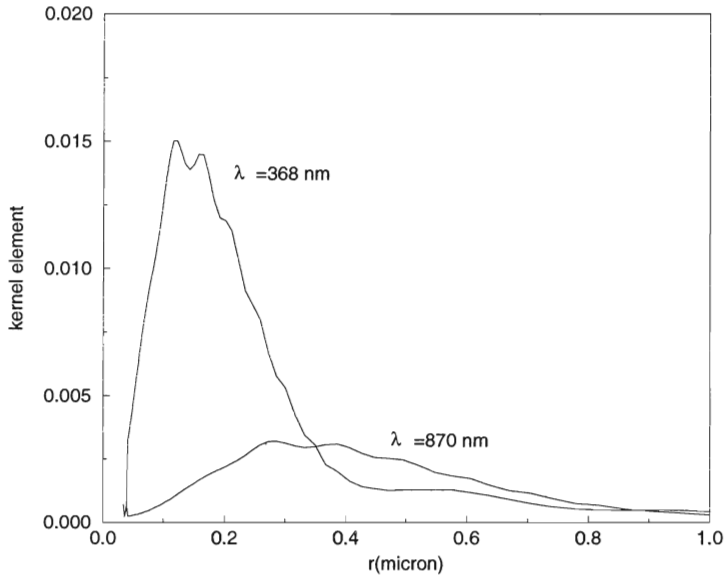

Figure 4: *Elements of kernelmatrix plotted against radius. The total radius interval has been divided in 50 parts.*

became worse but still positive solutions were found. The radius range depended slightly on the original distributions used for simulations, but for all simulations the size distribution could be retrieved for the interval between 0.1 μm – 0.8 μm. This radius range is used for evaluating the accuracy of the retrieval procedure.

4.3.2 Number of discrete sizes

As stated before, the number of discrete sizes, N, may exceed the number of wavelengths, M, at which measurements of the optical thickness are available. This is because in the algorithm of King et al. (1978) a priori information about the shape of the size distribution is introduced in the inversion procedure in the form of the power law. However, if N becomes too large, too much weight is given to this first guess size distribution. On the other hand, if N becomes too small, the assumption of a constant solution function $f(r)$ for each subinterval $[r_j, r_{j+1}]$ (see Eq. (19)) is no longer true. Therefore, an optimum value of N has to be chosen. Therefore, the inversion of the simulated optical thickness data is performed $N = 5$, 10 and 15. For both $N = 5$ and $N = 10$ the retrieved size distribution corresponded better to the original size distribution than for $N = 15$. Because it is desirable to retrieve $n(r)$ at many points, a value of N=10 is chosen to be the optimum.

4.3.3 Lagrange multiplier

King (1982) suggested to to vary γ_{rel} between values $\gamma_{rel}^{min} = 10^{-3}$ and $\gamma_{rel}^{max} = 1$ and to choose the lowest γ_{rel} for which all elements of the solution vector $\mathbf{f}$ are positive (see Sect. 3.5.2). However, most of the time this value appeared to be 10^{-3} and in some cases the solution seemed quite unstable. To

evaluate the influence of γ on the retrieved size distribution, inversions were applied to the simulated optical thickness for 3 different values: $\gamma_{rel}^{min} = 10^{-5}$, 10^{-3} and 10^{-1}. The value of γ_{rel}^{max} was not increased because values greater than 5 would give too much influence of the smoothing constraint. The results of inversions with 3 different values of γ_{rel}^{min} are shown in Fig. 5 a,b, and c for a two-parameter gamma distribution with $r_{eff} = 0.15$ μm and $v_{eff} = 0.2$.

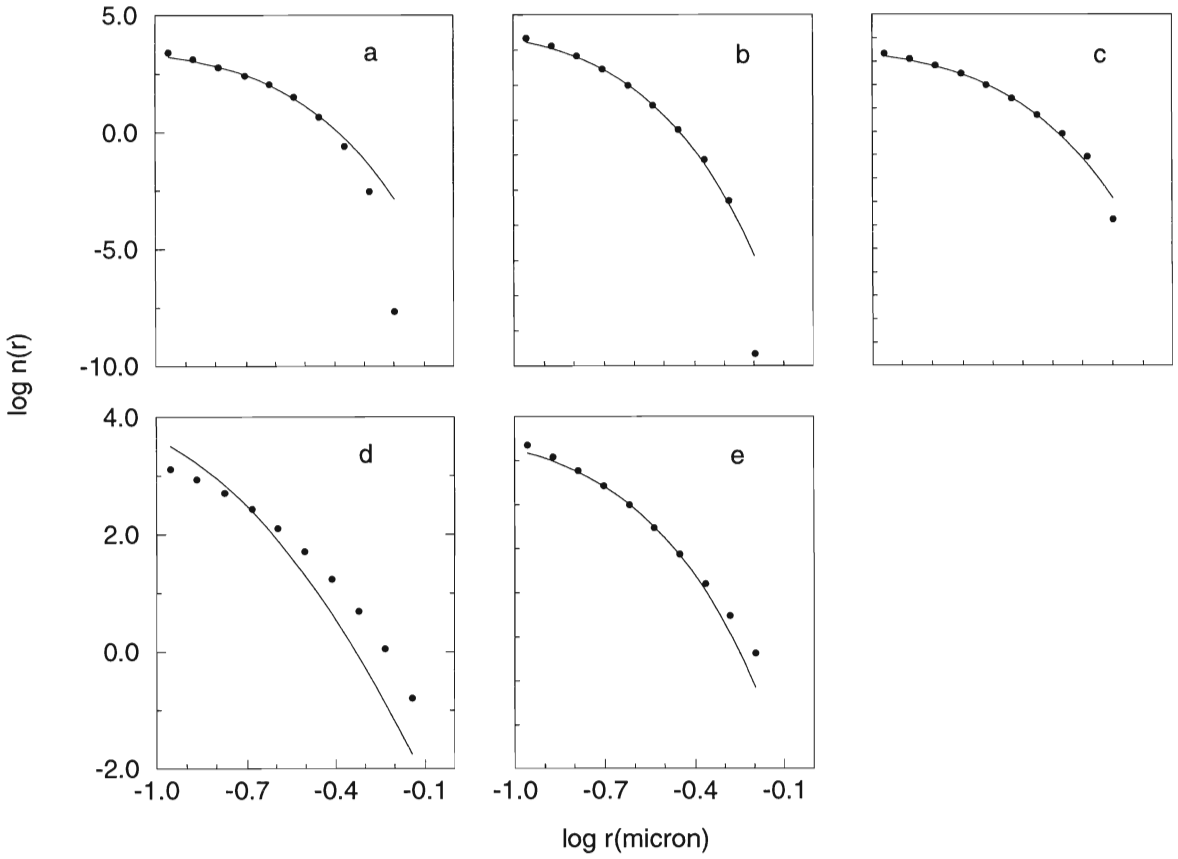

Figure 5: *a, b and c: Inversions for different minimum values of the Lagrange multiplier γ . The solid line is the original distribution, the dots represent the retrieved size distribution. a: $\gamma_{rel}^{min} = 10^{-5}$, b: $\gamma_{rel}^{min} = 10^{-3}$ and c: $\gamma_{rel}^{min} = 10^{-1}$. d and e: Inversion of simulated data for three wavelengths (368 nm, 670 nm and 780 nm). d: log-normal distribution with r_{eff}=0.13 μm and v_{eff}=0.30. e: two-parameter gamma with r_{eff}=0.15 μm and v_{eff}=0.25. $n(r)$ is in μm^{-2}.*

The inversion with $\gamma_{rel}^{min} = 10^{-5}$ clearly gives the worst result, while the inversion with $\gamma_{rel}^{min} = 10^{-1}$ gives the best result. Also for the other original distributions this was the case. The value $\gamma_{rel}^{min} = 10^{-3}$ lead most of the times to a unstable solution. However, it is important to notice that a large value of γ_{rel} leads to solutions with a relatively large influence of the smoothing constraint and a smaller influence of the measurements. This gives better results for perfectly smooth functions like the two parameter-gamma distribution and the log-normal distribution, but not necessarily for the real size distributions that occur in nature. Since a value for γ_{rel} of 10^{-1} is quite normal (King, 1982), this

value for γ_{rel}^{min} is chosen for the inversions made in this study.

4.3.4 Effect of the number of wavelengths

For most of the time of this study measurements of the aerosol optical thickness were available only at three wavelengths. Therefore, it is important to check if this small number of wavelengths is sufficient for retrieving the size distribution. The three available wavelengths were 368 nm, 670 nm and 780 nm. The effect of reducing the number of wavelengths on the inversion of the simulated data was studied for the three wavelengths mentioned above. The result is shown in Fig. 5 d and e for a log normal-distribution with r_{eff}=0.13 μm and v_{eff}=0.30 and a two-parameter gamma distribution with r_{eff}=0.15 μm and v_{eff}=0.25.

The size distributions shown in Fig. 5 differ a little from the corresponding distributions using five wavelengths, shown in Fig. 6 c and d, but it seems that the retrieval is not worse using only three wavelengths. The retrieved r_{eff} and v_{eff} have comparable values. The main problem of using only the three wavelengths mentioned is that the radius range is more limited. However, it has to be stated that this result is only valid for smooth original size distributions.

4.4 Accuracy of the retrieval procedure

With the optimal values found for the different parameters, a test of the inversion algorithm was performed. The size distributions used for the simulation were chosen in such a way that the optical thickness spectra, calculated with Mie theory, yielded realistic values for the Ångström parameter α, namely between 0.8 and 2.0. The distributions were:

Log normal-distributions with:

- $v_{eff} = 0.25$; r_{eff} is varied between 0.09 μm and 0.15 μm with steps of 0.01 μm
- $v_{eff} = 0.30$; r_{eff} is varied between 0.09 μm and 0.15 μm with steps of 0.01 μm

Two parameter gamma distributions with:

- $v_{eff} = 0.25$; r_{eff} is varied between 0.15 μm and 0.22 μm with steps of 0.01 μm
- $v_{eff} = 0.30$; r_{eff} is varied between 0.13 μm and 0.20 μm with steps of 0.01 μm

For some of these distributions the result of the inversion is shown in Fig. 6.

In these figures it can be seen that the retrieval is much better if the original size distribution is a two parameter gamma distribution. To get a quantitative impression of the goodness of the retrieval, it is useful to compare r_{eff} of the original distributions with r_{eff} of the inverted distributions. Therefore in Fig. 7 the correlation is shown between the original r_{eff} and the retrieved r_{eff}, where v_{eff} is kept constant.

For all four cases the correlation is linear, but deviates seriously from the $x = y$ line. The error in r_{eff} is partly an error in the retrieval method and partly an error due to the limited radius range of the retrieval. The error in the retrieval method can be evaluated when the retrieved r_{eff} is compared with the r_{eff} of the original distribution, now calculated for the radiusrange of the retrieval (see Sec. 4.3.1). This is done in Fig. 8 a and b. The differences between the retrieved r_{eff} and the original r_{eff} lie between 11% (small r_{eff}) and 25% (large r_{eff}) for the log-normal distributions. For the two-parameter gamma distributions these differences are always less than 3%. The differences between

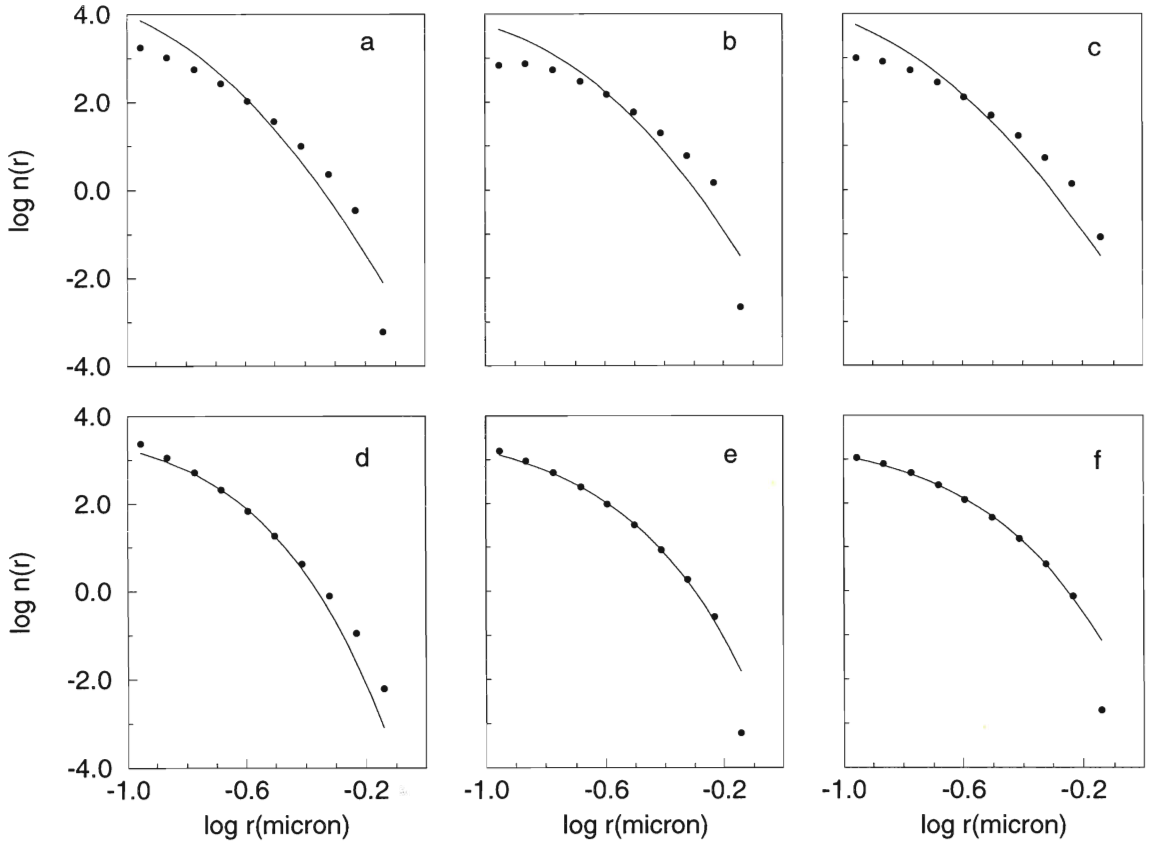

Figure 6: *Comparison of original size distributions (solid line) with distribution inverted from simulated data (dots). a-c: log-normal distributions. a:* $r_{eff} = 0.12\mu m$, $v_{eff} = 0.25$, *b:* $r_{eff} = 0.15\mu m$, $v_{eff} = 0.25$ *and c:* $r_{eff} = 0.13\mu m$, $v_{eff} = 0.30$. *d-f: two-parameter gamma distributions. d:* $r_{eff} = 0.15\mu$, $v_eff = 0.25$, *e:* $r_{eff} = 0.17\mu m$, $v_{eff} = 0.30$ *and f:* $r_{eff} = 0.20\mu m$, $v_{eff} = 0.30$. $n(r)$ *is in* μm^{-2}

the retrieved v_{eff} and the original v_{eff} are somewhat larger than they are for r_{eff} because the r_{eff} is used to calculate v_{eff}. However the differences for v_{eff} have about the same magnitude as they have for r_{eff}.

4.4.1 Extrapolation of the retrieved size distribution

The main cause of the difference between the retrieved r_{eff} and the original r_{eff} in Fig. 7 is the limited radius range of the retrieval. Because for the simulations, the retrieved r_{eff} is always larger than the original r_{eff}, it seems obvious that these differences are mainly a result of not taking into account the particles with $r < 0.1$ μm. Not taking into account the particles with $r > 0.8$ μm doesn't have much influence on the retrieved r_{eff}, because in most cases the size distribution is several orders of magnitude lower at 0.8 μm than it is at 0.1 μm. Figure 7 suggests that a simple correction can be applied to the to retrieved r_{eff} in order to get the real r_{eff}. Another (better) approach is to assume

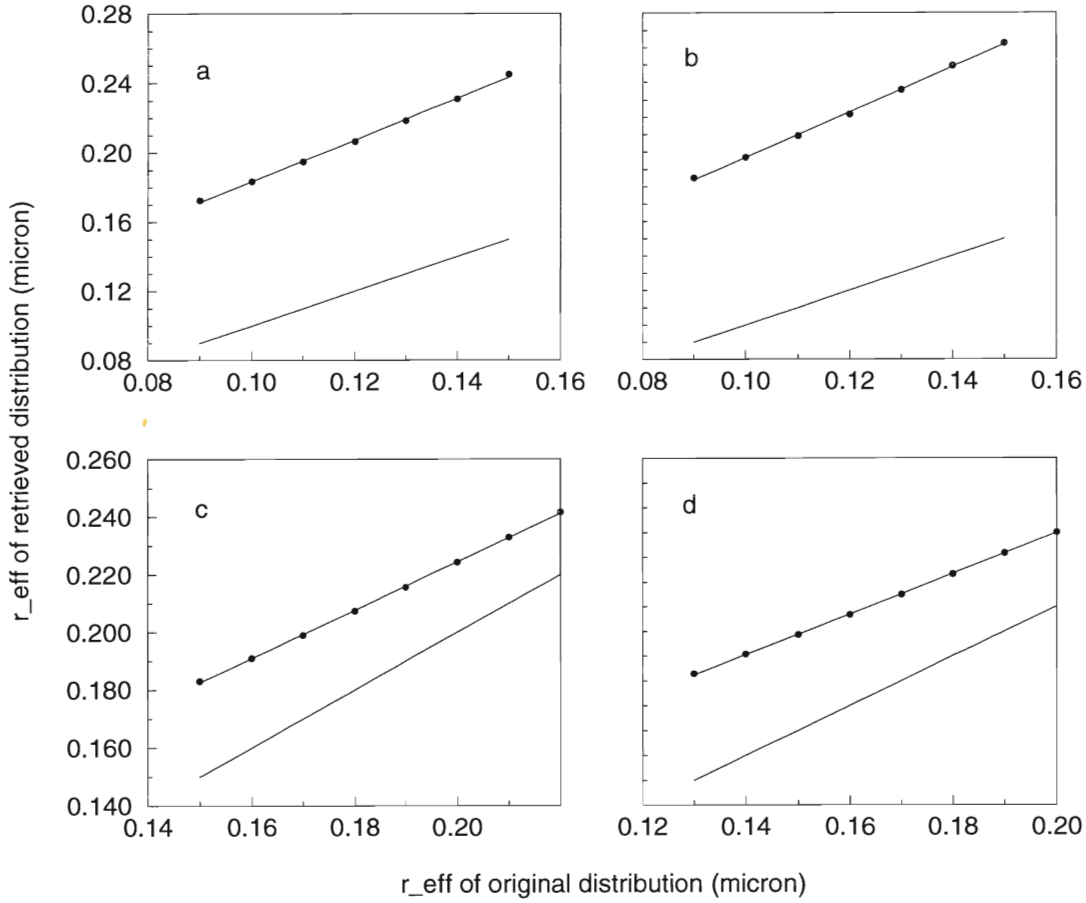

Figure 7: *Correlations between r_{eff} of the original distribution and r_{eff} of the retrieved distributions (dots). Figure a: log normal distribution with v_{eff}=0.25. Figure b: log normal distribution with v_{eff}=0.30. Figure c: two parameter gamma distribution with v_{eff}=0.25. Figure d: two parameter gamma distribution with v_{eff}=0.30. The solid line is the $x = y$ line*

a certain size distribution for $r < 0.1$ μm (i.e. extrapolating the retrieved size distribution to smaller sizes) in order to obtain a better value for r_{eff} and v_{eff}. In this study only the simplest way of extrapolating the size distribution is evaluated: extrapolating with the Junge power law (Eq. (15)) to r=0.01 μm. C and ν can be determined by requiring continuity of the function and its first derivative at the first point of the retrieved size distribution. The result of extrapolation with the Junge power law is shown in Fig. 8 c and d.

The error in r_{eff} due to the limited radius range of the retrieval is reduced for a great part by the extrapolation with a Junge power law to radii smaller than 0.1 μm. For the two-parameter gamma distribution the difference between the retrieved r_{eff} and the original r_{eff} is always less than 1.5% after the extrapolation. For the log normal-distribution however this difference is about 35%. This is about the same value as for Fig. 8 a. In all cases the extrapolation with the power law led to better results than cutting off the retrieved size distribution at 0.1 μm. Furthermore there is no reason for assuming zero particles at radii below 0.1 μm, since in most cases the maximum of the distribution was not yet reached at 0.1 μm.

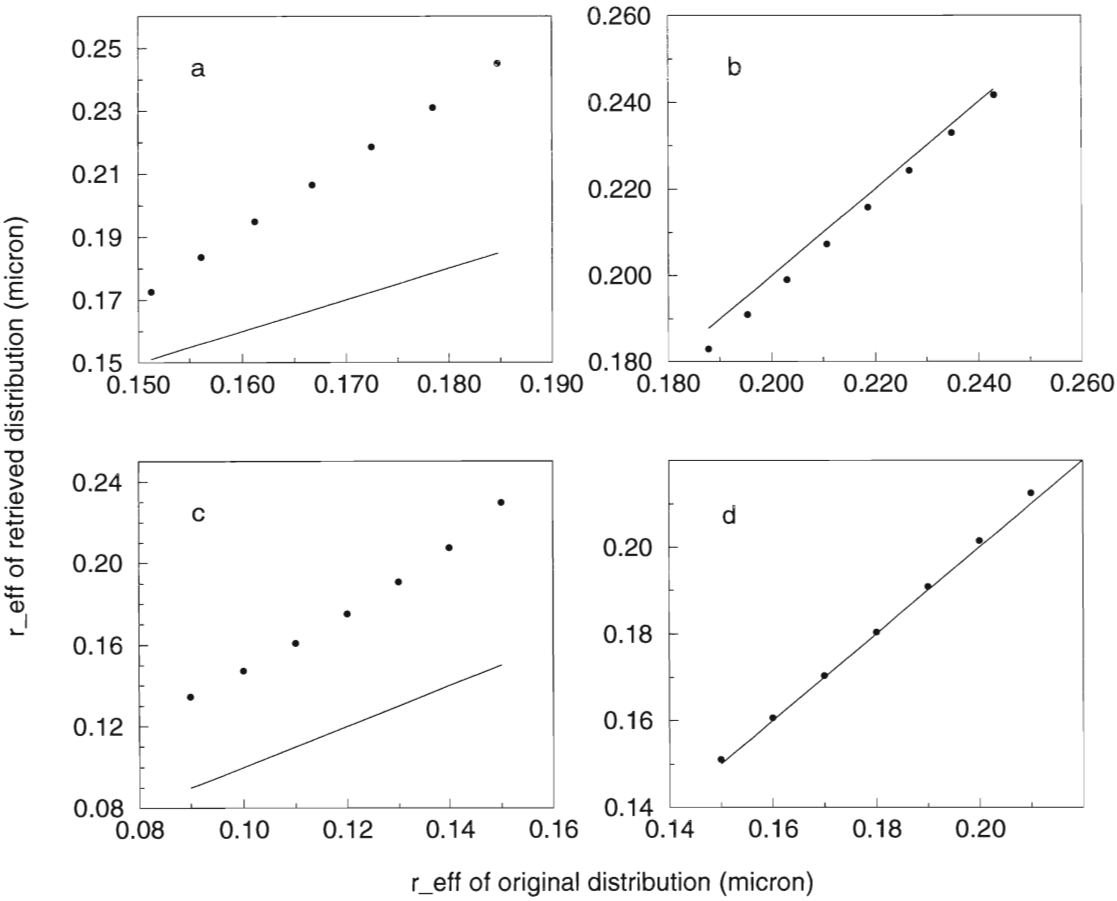

Figure 8: *Correlations between original r_{eff} and retrieved r_{eff}. a and b: original r_{eff} is calculated for radius range of the retrieval. c and d: Result for extrapolated size distributions. Log-normal distribution with v_{eff}=0.25 in a and c. Two-parameter gamma distribution on b and d. The solid line is the x=y line.*

4.5 Discussion

In most inversion problems three kinds of errors occur (Rodgers, 1990):

- An error due to measurement errors
- An error due to assumptions in the forward equation (Eq. (18)), like the sphericity of the particles and the refractive index
- The so called null space error due to the non-unicity of the solution

The differences between the retrieved distributions and the original distributions, used for simulation only gives indications for the null space error, because the influences on the solution of measurement-noise and assumptions in the forward equations are not evaluated in this study.

The retrieved distributions corresponded well to the original distributions when these were two-parameter gamma functions. However, if the original distribution was a log-normal distribution the retrieval was much worse. A reason for this could be that the constrained linear inversion method of

King et al. (1978) tends to produce narrow distributions, but further research is needed to get at a more satisfactory explanation.

For a accurate analysis of the different errors in the retrieved size distributions, the method of Rodgers (1990) should be applied.

5 Experimental setup

In this study a sunphotometer called the SPUV is used (Sun Photometer UV, Yankee environmental systems, type: SPUV-6). A dedicted data aquisition system, called the YESDAS (Yankee Environmental Systems Data Aquisition System), has been used. In this section the SPUV, the YESDAS and the terminal emulator programme are described. Also the startup problems of working with this new instrument are described.

5.1 The Sun Photometer UV

The SPUV is designed according to the WMO recommendations for sunphotometers (Fröhlich and London, 1986). Because it is placed on a sun tracker, it follows the sun all day. It measures the solar irradiance in six different channels as shown in Table 1.

channel	wavelength	width	purpose
1	368 nm	2.4 nm	aerosol
2	500 nm	15 nm	aerosol
3	670 nm	17 nm	aerosol
4	780 nm	14 nm	aerosol
5	870 nm	12 nm	aerosol
6	940 nm	14 nm	water vapour

Table 1: *Wavelengths of the SPUV channels and the belonging widths of the wavelength bands.*

In Fig. 9 a solar spectrum at ground level (including the atmospheric extinction) is shown together with the positions of the SPUV channels. In some of the aerosol channels there is influence of molecular absorption. The 368 nm channel is slightly influenced by NO_2 absorption and the 500 nm channel by ozone absorption. In the 670 nm channel the influence by ozone is more serious (Chappuis band). There is some weak water vapour absorption in the channels at 670 nm, 778 nm and 870 nm. The corrections for absorptions are explained in Sect. 5.3.1.

Each channel is an independently working unit with its own detector and amplifier. A cross section of a channel is shown in Fig. 10. The detectors are solid state photodetectors. The 368.5 nm channel has a GaP detector and the other channels have Silicon detectors. The filters used in each channel are state-of-the-art thin film interference filters. The 368 nm channel also has a 2 mm UG-11 UV transmission filter in order to minimize degradation of the interference filter from visible radiation. The output of each channel is a voltage that is proportional to the incident irradiance. A mechanical collimator in the channel assembly precisely limits the direct beam field of view to 2.5° (half angle, as described by Fröhlich and London (1986))

The irradiance measured in each channel is not the irradiance at one specific wavelength λ but integrated over a narrow wavelength band $\Delta\lambda$. The filter in each channel has a transmission function $c(\lambda)$, which is the fraction of the light transmitted at a wavelength λ. The central wavelength of each channel is given by:

$$\lambda_{eff} = \frac{\int_{\Delta\lambda} \lambda c(\lambda) d\lambda}{\int_{\Delta\lambda} c(\lambda) d\lambda}. \tag{42}$$

As an example, in Fig. 11 the transmission function is shown for the 780.4 nm channel. The maximum transmission is set to 1.0 in this figure. The wavelength bands of the channels should not be too wide because the variation of the solar irradiance, the atmospheric attenuation and the response of the diodes should be negligible within each wavelength band.

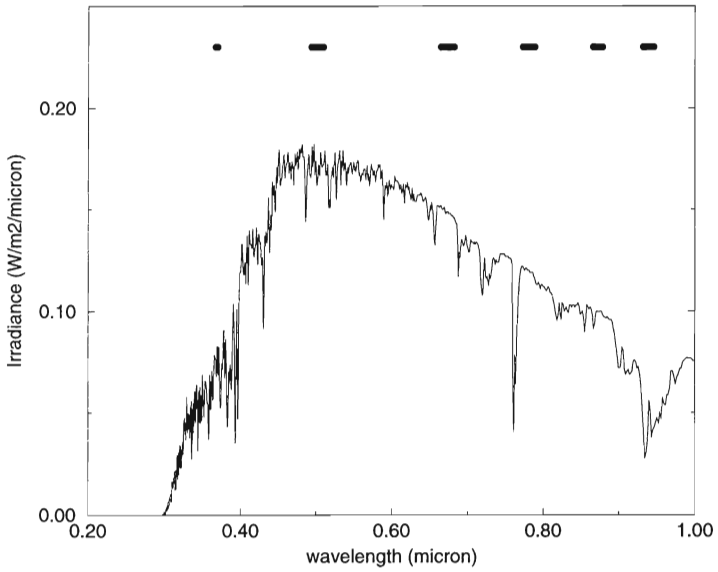

Figure 9: *Solar spectrum at surface level calculated by LOWTRAN for* $\theta_0 = 0°$. *The thick lines indicate the place of the SPUV channels*

Fröhlich and London (1986) state that one of the most important specifications for sun photometers is the demand for high temporal and operational stability. A weak temperature dependence exists for Silicon detectors, however, this dependence is almost zero at the central visible wavelengths. At the 870 nm and 940 nm channels there is a positive dependence of about 0.1%per K. The SPUV temperature is measured continuously and was always stable within 0.5 K during a Langley plot period. About the stability of the filters no information is given by the manufacturer. Fröhlich and London (1986) state that modern sun photometers with state-of-the-art filters are stable within about 1% at 368 nm and within 0.2% at 780 nm over a period of several years.

5.1.1 Data aquisition system

YESDAS is the data aquisition system connected to the SPUV. It receives the (analog) output voltages of the SPUV channels and converts these in to digital counts. YESDAS is connected to a computer at which a terminal emulator programme is installed, which is called YESTALK. In this way communication with YESDAS is possible. YESDAS must first be initialized, i.e. date, time, lattitude, longitude, sampling time and averaging time can be specified. In this study the sampling time was set at 5 seconds and the averages were stored once a minute. After initialization YESDAS is an independently working unit. It has its own clock and calculates the solar position during the day. In the YESDAS memory for every sample is stored: the daynumber in days since 1900, the dayfraction in UT, the cosine of the solar zenith angle, the voltage output of each SPUV channel and the internal temperature. If an averaging of the data is required, YESDAS only stores the average. The data can be downloaded to the computer with YESTALK. The only file transfering protocol that can be used for downloading data from the YESDAS is the *xmodem checksum* protocol. The down-loaded, raw

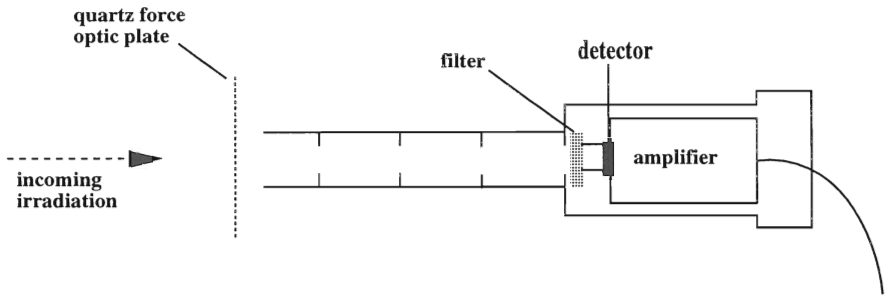

Figure 10: *Cross section of a SPUV channel*

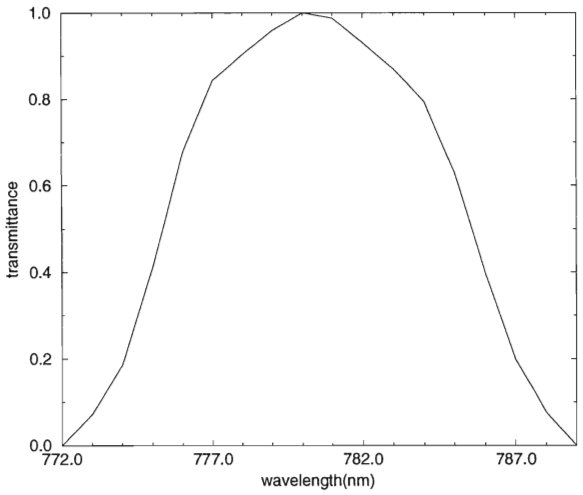

Figure 11: *Transmittance of the 780.4 nm channel*

data (voltages) can be used for further analysis.

5.1.2 Problems with the SPUV

When working with the SPUV several problems were encountered. Two important problems are discussed here

Saturation of SPUV channels

The analysis of the first few days yielded strange results for two of the six SPUV channels (500 nm and 870 nm). An example is shown for the 500 nm channel in Fig. 12. In this figure it can be seen that this channel is saturated when the incoming direct solar irradiance exceeds a certain value. This value corresponds to an output voltage of 3.6 V. The output of the detector is amplified too much. The problem was similar for the 870 nm channel. Therefore, these two channels had to be

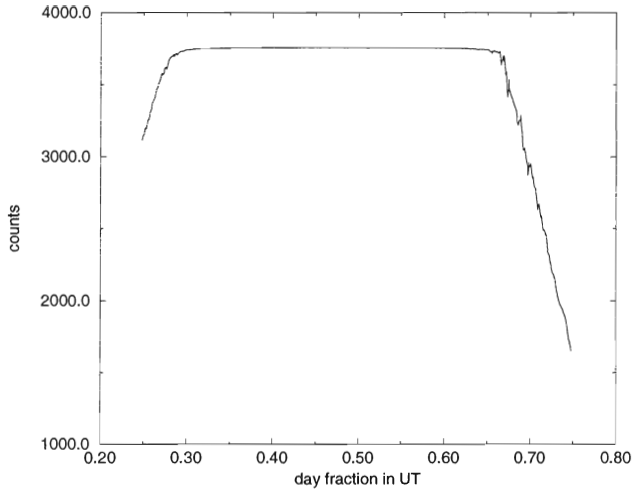

Figure 12: *Dayplot of the saturated 501.4 nm channel*

sent back to the manufacturer for repair. During most of the time of this study (July 1997 until January 1998) measurements were made with only four channels, of which one was the water vapour channel. Consequently, the aerosol optical thickness was measured at three instead of five wavelengths.

Size of the YESDAS memory

The YESDAS has a standard memory of only 32 KB. This means that when a sampling time of 10 seconds is used, the memory is full in three quarters of a day (in summer). With the YESTALK terminal emulator it was not possible to automatically download the data from the YESDAS to the computer at the end of each day. It was not possible to write a simple script in a programming language to perform this task, because YESDAS only accepts the *xmodem checksum* file transfer protocol, so a terminal emulator with a scripting language is needed for this. It appeared to be a problem that the *xmodem checksum* file transfer protocol is not commonly used. The terminal emulator with scripting language available at KNMI, called PROCOM PLUS, did not accept this protocol. Because of the limited YESDAS memory, the data were stored once a minute. Then it takes about three days until the memory is full. An expansion of the YESDAS memory to 2 MB has been ordered and will be placed in the YESDAS soon.

5.2 Calibration of the SPUV

The SPUV has been calibrated by the manufacturer by making use of a so called FEL lamp, of which the irradiance is known at several discrete wavelengths. Although this is the most accurate way for indoor calibration, still an uncertainty exists of about 10%. This uncertainty is due to:

- The signal to noise ratio of the FEL lamp is low, especially in the UV.
- The spectral output of the lamp is different from the spectral output of the sun. Variation exists in the irradiance of the lamp within the wavelength band of the SPUV-channels.

- The sun and the FEL lamp have different angular sizes.
- The provided spectral irradiance of the standard FEL lamp has a 5% uncertainty factor.

Harrison and Michalsky (1994) stated that the most accurate way of calibrating a sun photometer is the calibration by the Langley method. For calibration in this way it is important that only Langley plots are used, which correspond to stable clear sky conditions. With this method an uncertainty in the calibration can be obtained of less than 1 %, for which about 40 Langley plots are needed.

5.3 SPUV data analysis

One of the purposes of this study was to create a way of data analysis which is automatic for the greatest part. This means that from the raw data files (containing data for different days), which are downloaded from the YESDAS, only with a few actions the optical thickness for each day (divided in a morning and an afternoon part) must be obtained. It is important that the aerosol optical thickness obtained has a reliable value. It is also important that for the automatic removal of data points taken during cloud passages, an algorithm is chosen that works for all days. The SPUV data analysis consists of the following steps:

1. The raw datafiles contain data for different days. These files have to be split in different files for different days.
2. The files for the different days are split in morning and afternoon data. From these data only the data points between airmasses 2 and 6 are used. Then all the points are removed from which the measured direct irradiance in one of the channels is less than 10% of the extra terrestrial solar irradiance at the corresponding wavelength (according to the calibration of the manufacturer). This is the minimum level at which direct radiation can be distinguished from diffuse radiation which is also partly detected by the SPUV.
3. The next step is to remove datapoints that are taken during cloud passages. This is done by the method described in Sect. 2.2.2.
4. Linear regression is applied to the remaining datapoints. This regression results in a total optical thickness of the atmosphere and a value for the extra terrestrial solar irradiance $I_0(\lambda)$
5. To obtain the aerosol optical thickness $\delta_{tot}(\lambda)$ has to be corrected for Rayleigh scattering and molecular absorption (Eq. 9).

5.3.1 Corrections for gas absorption and Rayleigh scattering

In the aerosol channels the most important molecular absorptions take place by NO_2 (368 nm channel) and O_3 (500 nm and 670 nm channels). The corrections for NO_2 and O_3 absorption are performed using the DAK radiative transfer model. This model calculates for a standard gas profile (e.g. mid-latitude summer AFGL, 1986) the gas absorption optical thickness at the different wavelengths for many thin layers in the atmosphere. The contributions from all of these layers are added in order to find δ_g (Eq. (9)) of the total atmosphere. For the mid-latitude summer ozone profile the total ozone column equals: $OC^* = 334.02$ DU. At the KNMI the real ozone column (OC) is measured each day by a Brewer instrument. To find the ozone optical thickness for a particular day, $\delta_{oz}(\lambda)$, the optical thickness calculated by the DAK model is scaled according to the measured ozone column:

$$\delta_{oz}(\lambda) = \frac{OC}{OC^*}\delta^*_{oz}(\lambda). \tag{43}$$

The effect of variation of the ozone optical thickness within the wavelength band $\Delta\lambda$ of each SPUV channel has been evaluated and found to be negligible.

The optical thickness due to NO_2 absorption at 368 nm has been found to be 0.003. This is about 0.2% of the total optical thickness at 368 nm. No NO_2 measurements are available to scale this calculated value.

The Rayleigh scattering optical thickness $\delta^*_R(\lambda)$ is calculated by the DAK programme for the standard surface pressure p^*_{surf}=1013 Pa. The calculated $\delta^*_R(\lambda)$ is scaled according to the actual value of the surface pressure, which is measured at KNMI, to find $\delta_R(\lambda)$ (Eq. (9)):

$$\delta_R = \frac{p_{surf}}{p^*_{surf}}\delta^*_R. \tag{44}$$

Also for the Rayleigh optical thickness the effect of variation within the wavelength band of each SPUV channel has been evaluated and found to be negligible.

The values of $\delta^*_{oz}(\lambda)$, $\delta^*_{NO_2}(\lambda)$ and $\delta^*_R(\lambda)$ for each SPUV channel are tabulated in Table 2.

λ (nm)	$\delta^*_{oz}(\lambda)$	$\delta^*_{NO_2}(\lambda)$	$\delta^*_R(\lambda)$
368	0.00008	0.00301	0.50888
500	0.01411	0.00093	0.14021
670	0.01421	0.00006	0.04274
780	0.00258	0.00000	0.02355
870	0.00127	0.00000	0.01507
940	0.00127	0.00000	0.01106

Table 2: *Values of the optical thickness due to gas absorption and Rayleigh scattering for the SPUV channels.*

6 Results

6.1 Measurements of the optical thickness

Measurements have been made in De Bilt (latitude=52.1°, longitude=−5.18°) from half July until half November (1997) at 4 wavelengths (see Sect. 5.1). In this period, 29 Langley plots (24 morning and 5 afternoon) could be made for all four channels, according to the cloud removal algorithm. The best clear sky conditions were obtained in August. In Table 3 the Langley analysis results are shown for the 780 nm channel. It is remarkable that even on the day with the best clear sky conditions

date	%	σ	$\ln I_0$	σ_{ex}	δ_{tot}	σ_δ	δ_{aer}	α	σ_α
970711 am	36.0	0.01097	0.28496	0.00388	0.12617	0.00105	0.10003	1.67773	0.0082116
970723 am	11.8	0.00972	0.15236	0.00720	0.13483	0.00160	0.10870	1.77867	0.0552254
970728 am	12.5	0.03517	0.33100	0.02909	0.16839	0.00728	0.14226	1.73677	0.1001679
970804 am	10.0	0.07218	0.58088	0.08771	0.32992	0.02189	0.30386	0.69789	0.1774237
970806 am	36.3	0.00623	0.25426	0.00216	0.09601	0.00063	0.07000	1.49734	0.0471307
970808 am	28.1	0.02221	0.41533	0.01520	0.17990	0.00391	0.15381	1.31536	0.0044881
970809 am	47.8	0.00338	0.20976	0.00134	0.09881	0.00035	0.07273	1.73761	0.0600518
970810 am	22.2	0.01301	0.30475	0.01245	0.22964	0.00387	0.20358	1.74238	0.0867314
970811 am	17.0	0.01758	0.20765	0.01144	0.10278	0.00351	0.07670	1.96908	0.2984379
970811 pm	25.7	0.00563	0.26179	0.00999	0.11062	0.00402	0.08453	1.55605	0.1110725
970812 am	15.6	0.00136	0.24259	0.00321	0.09231	0.00062	0.06618	1.48704	0.0822526
970812 pm	16:4	0.00749	0.21020	0.02392	0.13667	0.00913	0.11053	1.65961	0.0542262
970813 am	8.9	0.01673	0.21824	0.01184	0.13697	0.00295	0.11089	1.77323	0.0353859
970820 am	40.4	0.02311	0.30054	0.01030	0.22894	0.00260	0.20283	1.77860	0.0734541
970824 am	8.8	0.02994	0.88366	0.04254	0.54197	0.01377	0.51610	1.15363	0.0896024
970901 am	6.5	0.00944	0.29390	0.01494	0.13600	0.00387	0.11021	1.36113	0.0760334
970903 am	10.7	0.04089	1.09581	0.06649	0.63039	0.02187	0.60466	0.82490	0.2118932
970910 am	9.4	0.00762	0.24258	0.01066	0.11392	0.00237	0.08815	-0.16444	0.0624949
970926 am	7.5	0.00658	0.44057	0.02289	0.16898	0.00906	0.14322	1.42928	0.0372192
970926 pm	9.5	0.01126	0.21174	0.02549	0.09322	0.01044	0.06745	1.42492	0.1153781
971018 am	7.9	0.00621	0.24919	0.00547	0.06650	0.00132	0.04064	1.12857	0.2743580
971019 am	7.6	0.02155	0.48893	0.01544	0.23402	0.00466	0.20808	1.01551	0.1409534
971021 am	11.8	0.00113	0.31187	0.00140	0.06160	0.00040	0.03569	1.55588	0.2072317
971022 am	18.6	0.00246	0.29419	0.00163	0.05272	0.00039	0.02704	1.53757	0.2792874
971022 pm	6.8	0.00105	0.28204	0.00318	0.04969	0.00116	0.02401	1.63474	0.3548557
971027 am	21.7	0.00191	0.30898	0.00128	0.05253	0.00031	0.02870	1.31809	0.2050010
971104 am	15.4	0.00283	0.27145	0.00198	0.06388	0.00046	0.04009	1.63412	0.2380716
971104 pm	11.8	0.00268	0.26684	0.01880	0.06848	0.00644	0.04469	1.14092	0.1825240
971109 am	5.7	0.01430	0.47147	0.02118	0.14093	0.00440	0.11717	0.36445	0.0255026

Table 3: *Langley analysis results of 4 months in 1997. "%" means the percentage of points remaining after removal of clouds, σ is the standard deviation of the regression fit, σ_{ex} is the standard deviation in $\ln I_0$, σ_δ is the standard deviation in δ_{tot} and σ_α is the standard deviation in α. I_0 is in $(Wm^{-2}nm^{-1})$ with calibration of manufacturer.*

(97-08-09) only 48% of the initial data points remain after filtering with the cloud removal algorithm. In Table 3 it can be seen that this percentage mostly lies below 20%.

6.1.1 Measurements of a single day

To illustrate the direct sun measurements and Langley analysis for a representive day, Fig. 6.1.1 shows day plots (irradiance measurements) and Langley plots for all four SPUV channels for the morning of the 10th of August, 1997.

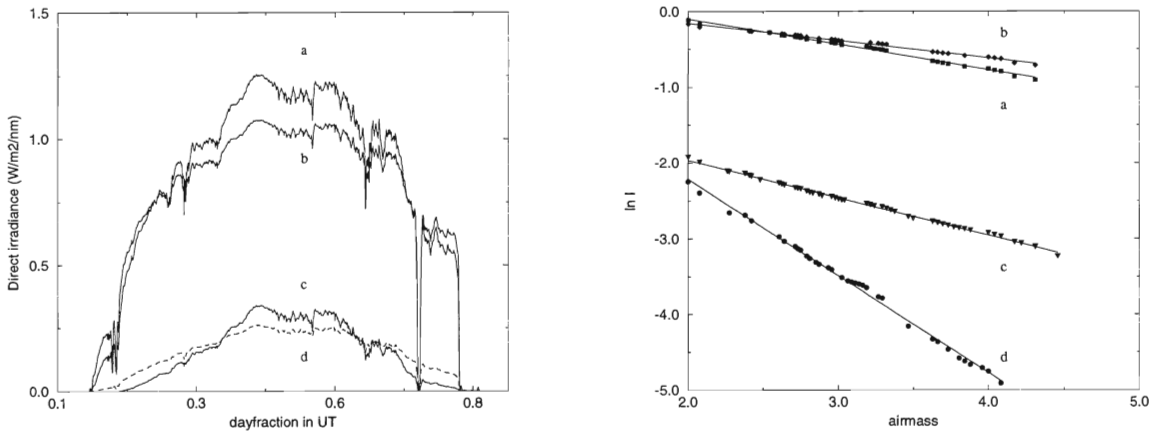

Figure 13: *Results for the 10th of August. Left: day plots, right: Langley plots. a: 670 nm channel, b: 780 nm channel, c: 940 nm channel, d: 368 nm channel*

This was a day with partly clear sky conditions, which also can be seen from the day plot in Fig. 13. The points with $m_r > 4$ are rejected by the cloud removal algorithm because $\delta(\lambda)$ seems to increase in this period.

6.1.2 Quality of the retrieval

To get an idea of the quality of the Langley analysis, it is useful to look at the intercept with the $\ln I$-axis in the Langley plot. Because this intercept represents the value $\ln I_0$, it must have the same value for all days at which Langley plots are made (after correction for the Sun-Earth distance). Another measure for the quality of the Langley analysis is the standard deviation of the Langley regression fit, σ. Both quantities are shown versus day number in Fig. 14. In this figure it can be seen that quite some variation exists in the value found for $\ln I_0$ for the different days. However, the relative differences in $\ln I_0$ for the different days can partly be explained because the value of $\ln I_0$ is close to zero. In most cases where this value differs much from the average value the standard deviation of the regression fit is quite big. As expected, these are often the days when only a small percentage of the original data points remain after filtering. If only the best days (e.g. $\sigma < 0.01$ and percentage higher than 10%) are used, the deviation of $\ln I_0$ between the different days reaches a value of 0.1.

The three values of the aerosol optical thickness, for which $\ln I_0$ deviates the most from the average, corresponding to the Langley plots of 97-08-04, 97-08-24 and 97-09-03, are not considered to be reliable. The rest of the results are stored in an optical thickness data base. From these results, some are more reliable than others, as is indicated by σ and σ_δ.

The I_0 for the different wavelengths, as was found by the Langley method, was in all cases larger

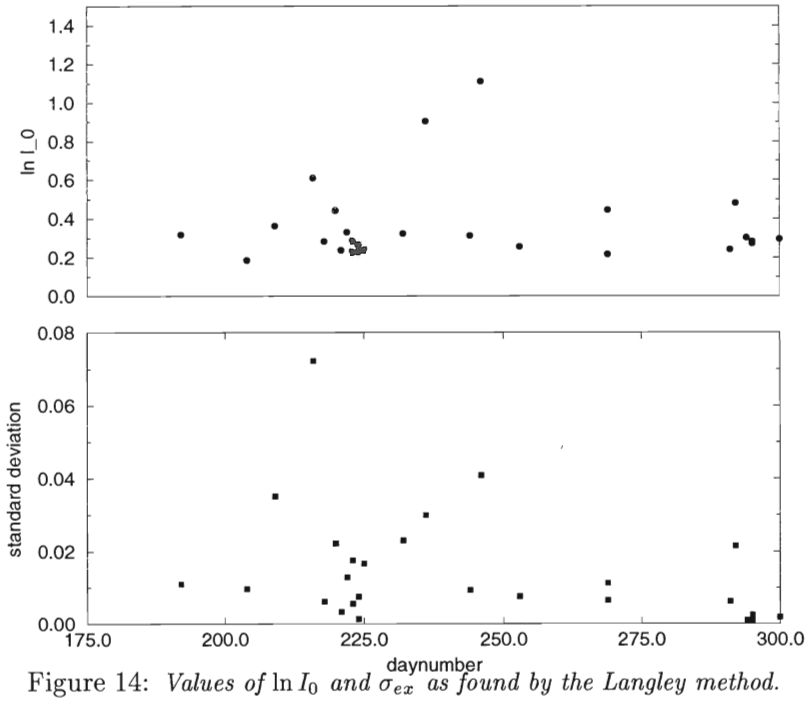

Figure 14: *Values of* $\ln I_0$ *and* σ_{ex} *as found by the Langley method.*

than the real value. It seems that this is the result of a calibration error. After rejecting the three cases mentioned above, the standard deviation in I_0 for the different days reduced to about 7%. These values of I_0 can be used for calibration. However, for an accurate calibration much more Langley plots are needed. Once accurate values for the calibration constants are determined, it is possible to determine the daily variation of the optical thickness in order to get optical thickness information at days with an unstable atmospheric conditions. With the calibration information of the FEL lamp this is not useful. From Eq. (11) follows:

$$\Delta\delta(\lambda) = \Delta \ln I(\lambda) = \frac{\Delta I(\lambda)}{I(\lambda)}, \tag{45}$$

since the dominant error in Eq. (11) is the error in $\ln I$. From Eq. (45) it follows that an uncertainty of 10% in the measured irradiances $I(\lambda)$ leads to an error of about 40% in the retrieved optical thickness (for the 780 nm channel)

The errors in $\delta_a(\lambda)$, found by the Langley method, are a result of:

- An error in the measured irradiance. The manufacturer assures a linearity of better than 1%. Another error in the measured irradiance is caused by the pointing error of the suntracker. However, if the the suntracker is following the sun correctly within 1°, this effect is negligible.

- An error due to instability. This can be instrumental (see sect.5.1) or atmospheric instability. In this study the error due to instrumental instability is assumed negligible compared to the error due to atmospheric instability.

- An error in the correction for ozone absorption. The error in the ozone column measured by the Brewer (and thus the error in the ozone optical thickness) is about 3%.

- An error due to forward scattering by aerosols (see Sect. 6.1.3).

The standard deviation in the slope of the Langley plot is a good measure of the error in the retrieved total optical thickness, because it includes both instrumental errors and errors due to atmospheric instability. The standard deviation in $\delta_a(\lambda)$ lied most of the times between 1 and 3 %. Systematic errors, e.g. caused by changes in time of the transmittance of the filters in the SPUV channels, are not included in the standard deviation. These errors can be traced by trends in the found $\ln I_0(\lambda)$.

The influence of the error in the ozone correction is found to be negligible (about 0.01 % of the retrieved aerosol optical thickness) in comparison with the standard deviation. This even holds for the 670 nm channel where the ozone absorption optical thickness has the greatest value.

6.1.3 Error due to aerosol forward scattering

Because a part of the measured irradiance is not direct solar irradiance but irradiance due to forward scattering by aerosols, the derived values for the optical thickness are underestimated (aureole effect). This effect is different for the different SPUV-channels and for different aerosol size distributions, because the forward peak increases when the aerosols are large compared to the wavelength. According to Fröhlich and Quenzel (1974) the value of $\delta_a(\lambda)$ is overestimated by a value $\Delta^{aur}\delta_a(\lambda)$, given by:

$$\Delta^{aur}\delta(\lambda) = \frac{1}{m_r} \ln\left(1 + \frac{I_{aur}(\lambda)}{I(\lambda)}\right), \tag{46}$$

where $I_{aur}(\lambda)$ is the irradiance due to forward scattering. This expression accounts for the case that $\delta(\lambda)$ is determined from one calibrated measurement of $I(\lambda)$. The fraction of singly scattered light in a 5° solid angle around the sun (field of view of SPUV-channels) is calculated according to Mie theory. This was done for log-normal and two-parameter gamma distributions which yielded normal values for α.

From these calculations it was estimated that for large effective sizes (α=0.9), the error due to the aureole effect was about 0.4% for λ=368 nm and 0.2% for λ=870 nm. For small effective sizes (α = 1.8) this error was estimated at 0.3% for λ=368 nm and 0.1% for λ=870 nm. For the other wavelengths the errors lie between the values for these two wavelengths. For these estimations a value of m_r=4 is chosen in Eq. (46), because this is the mean value of m_r for the Langley plots made in this study. In the future, correction for the aureole effect should be applied to the derived values of $\delta(\lambda)$.

6.2 Time series

The measurements made in the period of 108 days between half July and half November 1997 resulted in the time series of the aerosol optical thickness presented in Fig. 15. In Fig. 15 it can be seen that the aerosol optical thickness is very variable with time. For the 670 nm SPUV channel δ_a varies between about 0.03 and 0.3, a difference of one order of magnitude.

6.2.1 Discussion of selection effects

As stated before, Langley analysis can only be applied when the optical thickness is constant during a certain period of a day. The time series presented here, does not give a complete picture of the aerosol properties for the period between July and November 1997, because only values of the aerosol optical thickness are determined for *parts* of days with clear sky conditions for which the aerosol optical thickness did not change during the period of the Langley plot. This is all that can be achieved with an uncalibrated sunphotometer. Therefore, an accurate calibration of the SPUV is needed. Then,

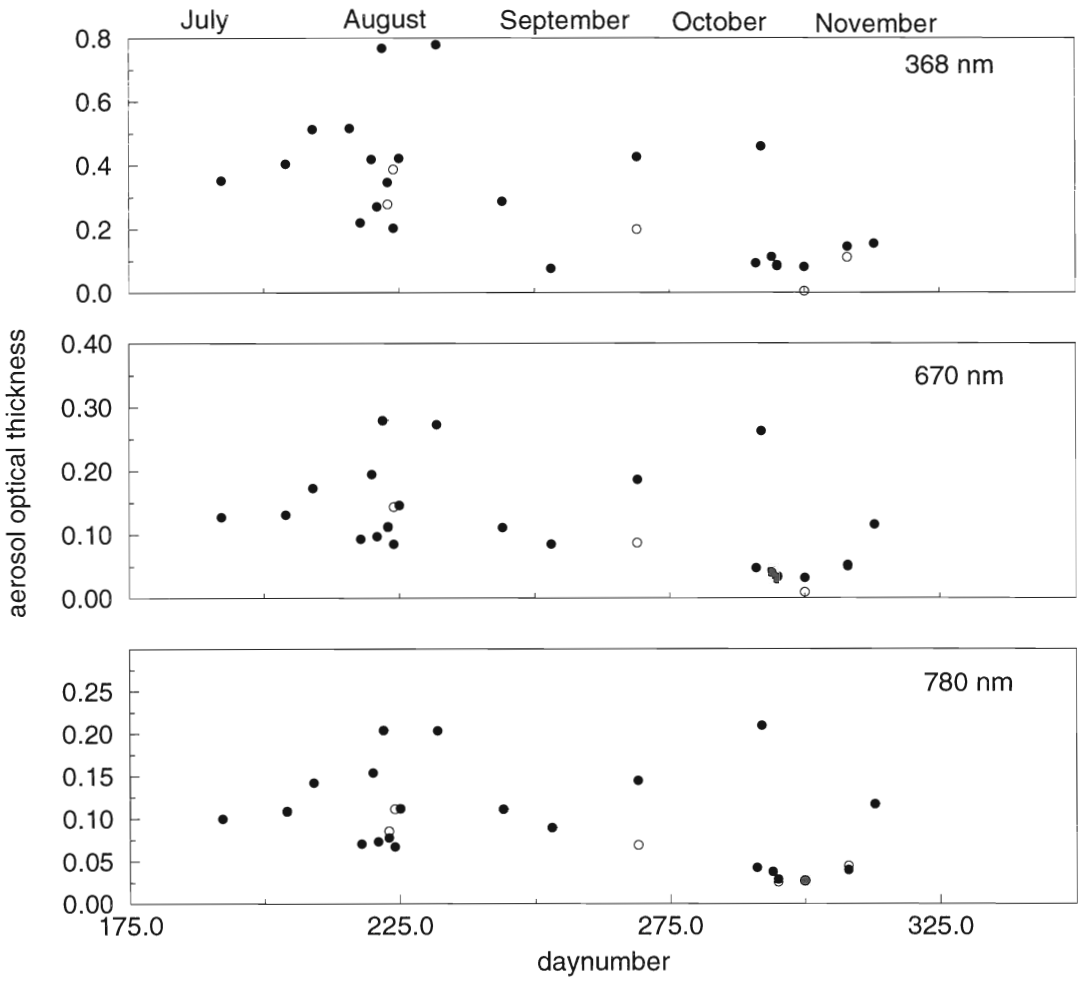

Figure 15: *Time series of the aerosol optical thickness at 368 nm, 670 nm and 780 nm. The open circles correspond to afternoon measurements.*

all clear sky moments of a day can be used to determine the aerosol optical thickness with Eq. (11). More fluctuations in $\delta_a(\lambda)$ are expected to be seen then, because measurements taken at different atmospheric conditions can be used.

6.3 Retrieved size distributions

For all days at which measurements of the optical thickness are available the aerosol size distribution has been retrieved. In Fig. 16 some typical size distributions for the four months of measurements are shown.

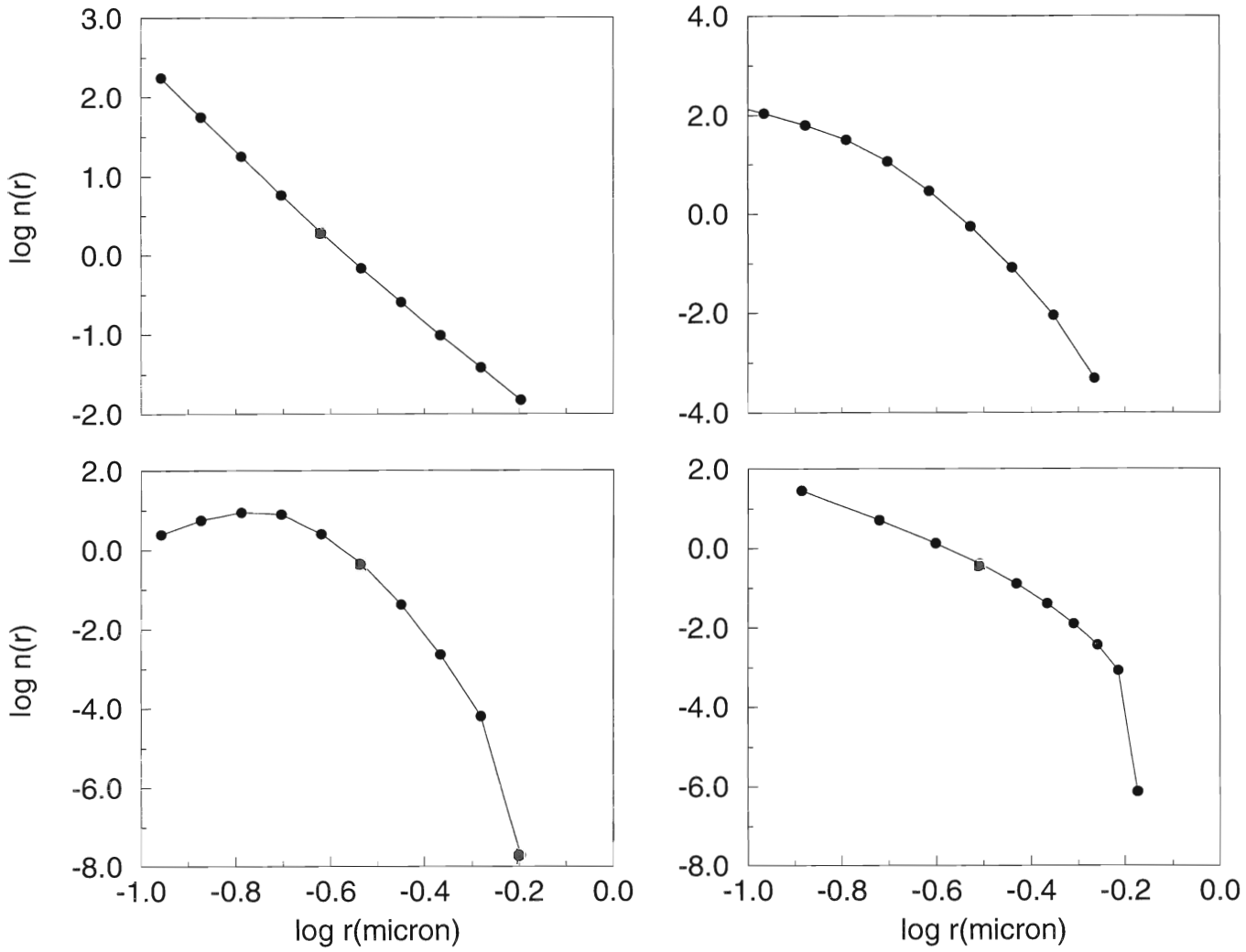

Figure 16: *Size distributions for 4 days in 1997: August 9 (upper left), August 11 (upper right), October 18 (lower left) and November 4(lower right). $n(r)$ is in μm^{-2}.*

To characterize the aerosols for different days it is informative to consider r_{eff} and v_{eff} of all retrieved size distributions. In Fig. 17 time series are shown of these quantities for the retrieved distributions, extrapolated with the Junge power law (see Sect. 4.4.1). In Fig. 17 it can be seen that in the summer (July and August) the retrieved size distributions have a relatively small r_{eff} and large

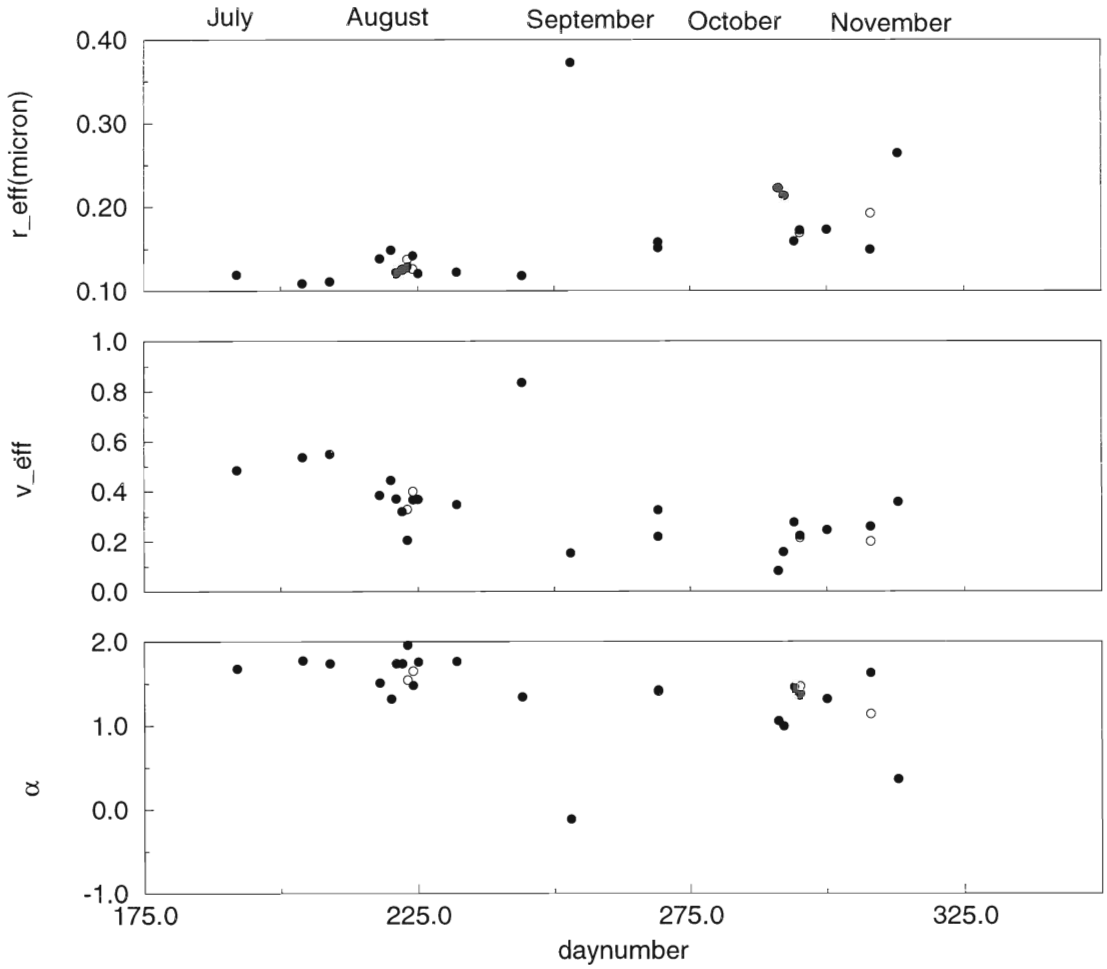

Figure 17: *Upper and middle figure: Time series of r_{eff} and v_{eff} for the retrieved distributions, extrapolated with the Junge power law. Lower figure: time serie of the Ångström parameter α. The open circles correspond to afternoon measurements.*

v_{eff} in comparison with the aerosol size distributions retrieved in October and November. This result can be explained by the fact that small aerosols mostly correspond to polluted air (anthropogenic aerosols) while large aerosols mostly correspond to clean air. In summer the air is known to be most polluted. In Fig. 15 it can be seen that in summer the aerosol optical thickness is relatively large which is also an indication of polluted air. In Fig. 17 also the time series is given of the Ångström parameter α (Eq. (12)). This time series correspond well to the time series of r_{eff} and v_{eff}: if α increases, the effective particle size decreases.

7 Conclusions and future work

Cloud passages often disturb the clear sky conditions, needed for Langley analysis of sunphotometer data. The new algorithm, proposed here, for the automatic removal of cloudy data points from the data set, works well for measurements taken in De Bilt. However, the number of useful days for Langley analysis is still limited. In 5 months of measurements only 26 mornings and afternoons were found to be useful for Langley analysis. Therefore, an accurate calibration of the SPUV is needed in order to retrieve the aerosol optical thickness with a single measurement and to obtain information about the daily variation of the aerosol optical thickness. Then, more representive time series of aerosol characteristics could be made. The time series, presented in this report, are only based on days with (partly) clear sky conditions. The calibration information available about the SPUV is only accurate within 10%. This would lead to errors of more than 30% in the optical thickness, derived from one calibrated measurement. With the Langley method a calibration can be obtained with an error of less than 1%. However, more Langley plots are needed for this than available now.

From the inversion of simulated optical thickness data it follows that the retrieval of the aerosol size distribution is good when the actual size distribution looks like a two-parameter gamma function. However, the retrieval is worse when the actual distribution looks like a log-normal function. The reason for this should be object of future research. It seems that the aerosol size distribution is not uniquely defined by multispectral measurements of the aerosol optical thickness. Another problem is that the size distribution can only be retrieved in a limited radius range (0.1 μm–0.8 μm). For retrieval of the effective radius r_{eff} and effective variance v_{eff} the greatest problem seems to be caused by not taking into account particles with radii smaller than 0.1 μm. Extrapolation with the Junge power law to smaller sizes led always to better results for r_{eff} and v_{eff}. More information is needed to retrieve the size distribution outside the given radius range. This information could come e.g. from measurements of diffuse sky light (e.g. aureole, almucantor) or polarisation.

In this study only an indication of the error in the retrieved size distributions due to non-uniqueness is given. Errors due to assumptions in the forward model and due to measurement errors are not evaluated. However, these errors may be important. Therefore, in future a complete error analysis should be applied to the inversion algorithm.

From the time series presented in this report it follows that the aerosol optical thickness $\delta_a(\lambda)$ in De Bilt is very variable in time. At 670 nm $\delta_a(\lambda)$ varied between 0.03 and 0.3. In the summer (July and August) the aerosol optical thickness was most of the time larger than in the autumn (October and November). The values found for r_{eff} varied between 0.1 μm and 0.4 μm. In the summer months this value was most of the time smaller than it was in the autumn months. In future, the aerosol properties found in this study could be correlated with e.g. wind direction.

References

Ångström, A.(1930), "On the atmospheric transmission of Sun radiation II", *Gegr. Ann.*, **12**, 1301

Chahine, M.T. (1972), "A general relaxation method for inverse solution of the full radiative transfer equation", *J. Atmos. Sci*, **29**, 741-47.

Chu, W.P. (1985), "Convergence of Chahine's nonlinear relaxation inversion method used for limb viewing Remote sensing", *Appl. Opt.* , **24** , 445-47.

Fröhlich, C., and H. Quenzel (1974), "Inluence of the Sun's aureole on the determination of turbidity", *WMO publication*, **368**: 538

Fröhlich, C., and J. London (eds.) (1986), *Revised instruction manual on radiation instruments and measurements*, WCRP Pub. Series No.7. WMO/TD. No. 149, 140 pp

Hansen, J.E. and L.D. Travis (1974), "Light scattering in planetary atmospheres", *Space Sci. Rev.*, **16** , 527-610.

Hansen, J.E. and A.A. Lacis (1990), "Sun and dust versus greenhouse gases: An assesment of their relative roles in global climate change", *Nature*, **346**, 713-719.

Harrison, L. and J. Michalsky (1994), "Objective algorithms for the retrieval of optical depths from ground-based measurements", *Appl. Opt.*, **33**, 5126-5132.

Heintzenberg, J., H. Müller, H. Quenzel and E. Thomalla (1981), "Information content of optical data with respect to aerosol properties with a randomized minimization-search technique inversion algorithm", *Appl. Opt.*, **20**, 1308-1315.

Herman, M., J.L. Deuzé, C. Devaux, P. Goloub, F.M. Bréon and D. Tanré (1997), "Remote sensing of aerosols over land surfaces including polarisation measurements and application to POLDER measurements", *J. Geophys. Res.*, D, **14**, 039-049.

Jorge, H.G. and J.A. Ogren (1996), "Sensitivity of retrieved aerosol properties to assumptions in the inversion of spectral optical depths", *J. Atmos. Sci.*, **53**, 3669-3683.

Kasten, F. (1966), "A new table and approximate formula for relative airmass" , *Arch. Meteorol. Geophys. Bioklimatol. Ser.B*, **14**, 206-223.

Kasten, F. and A.T. Young (1989), "Revised optical airmass tables and approximation formula", *Appl. Opt.*, **28**, 4735-4738.

King, M.D., D.M. Byrne, B.M. Herman and J.A. Reagan (1978), "Aerosol size distributions obtained by inversion of spectral optical depth", *J. Atmos. Sci.*, **35**, 2153-2167.

King, M.D. (1982), "Sensitivity of constrained linear inversions to the selection of the Lagrange multiplier", *J. Atmos. Sci.*, **39**, 1356-1369.

Lenoble, J. (1984), "A general survey of the problem of aerosol climate impact. In: "Aerosols and their climate effects". H.E. Gerber and A. Deepak (eds.), A. Deepak Publ., Hampton Virginia, USA, 279-294.

Lenoble, J. (1993), *Atmospheric radiative transfer*, A. Deepak Publ., Hampton Virginia, USA.

Liebelt, P.B. (1967), *An introduction to estimation theory*, Addison-Wesley.

McClatchey, R.A., R.W. Fenn, J.E.A. Selby, F.E. Volz and J.S. Garing (1972), "Optical properties of the atmosphere (third edition)", AFGL Environmental Research Papers No. 411, Hanscom, MA.

Phillips, D.L. (1962), "A technique for the numerical solution of certain integral equations of the first kind", *J. Assoc. Comput. Mach.*, **9**, 84-97.

Press, W.H., S.A. Teukolsky,W.T. Vettering, B.P. Flannery (1992), *Numerical recipes in Fortran. The art of scientific computing*, Cambridge University Press.

Radiation Commission of IAMAP (1986), A preliminary cloudless standard atmosphere for radiation computation, WCP-112, WMO/TD No. 24, 53pp.

Rodgers, C.D. (1976), "Retrieval of atmospheric temperature and composition from remote measurements of thermal radiation", *Rev. Geoph. Space Physic*, **14**, 609-624.

Rodgers, C.D. (1990), "Characterization and error analysis of profiles retrieved from remote sounding measurements", *J. Geophys. Res.*, D, **95**, 5587-5595.

De Rooij, W.A. and C.C.A.H. Van der Stap, "Expansion of Mie scattering matrices in generalized spherical functions", *Astron. Astrophys.*, **131**, 237-248, 1984.

Twomey, S. (1977), *Introduction to the mathematics of inversion in remote sensing and indirect measurements.* Elsevier, Amsterdam, The Netherlands.

Wauben, W.M.F. (1996), "A new algorithm for total ozone retrieval from direct sun measurements with a filter instrument", KNMI, Scientific Report WR-96-01, De Bilt.

KNMI-Publicaties, Technische & Wetenschappelijke Rapporten, gepubliceerd sedert 1995

Een overzicht van eerder verschenen publicaties, wordt verzoek toegezonden door de Bibliotheek van het KNMI, postbus 201, 3730 AE De Bilt, tel. 030 - 2 206 855, fax. 030 - 2 210 407; e-mail: biblioth@knmi.nl

▼ KNMI-PUBLICATIE MET NUMMER

150-28 Sneeuwdek in Nederland 1961-1990 / A.M.G. Klein Tank
176-S Stormenkalender: chronologisch overzicht van alle stormen (windkracht 8 en hoger) langs de Nederlandse kust voor het tijdvak 1990-1996 / [samenst. B. Zwart ea.]
180a List of acronyms in environmental sciences : revised edition / [compiled by P. Geerders and M. Waterborg]
181a FM12 SYNOP : internationale en nationale regelgeving voor het coderen van de groepen 7wwW1W2 en 960ww
181b FM12 SYNOP : internationale en nationale regelgeving voor het coderen van de groepen 7wwW1W2 en 960ww; derde druk
183-1 Rainfall in New Guinea (Irian Jaya) / T.B. Ridder
183-2 Vergelijking van zware regens te Hollandia (Nieuw Guinea), thans Jayapura (Irian Jaya) met zware regens te De Bilt / T. B. Ridder
183-3 Verdamping in Nieuw-Guinea, vergelijking van gemeten hoeveelheden met berekende hoeveelheden / T.B. Ridder
183-4 Beschrijving van het klimaat te Merauke, Nieuw Guinea, in verband met de eventuele vestiging van een zoutwinningsbedrijf / T.B. Ridder ea.
183-5 Overzicht van klimatologische en geofysische publikaties betreffende Nieuw-Guinea / T.B. Ridder
184 Inleiding tot de algemene meteorologie : studie-uitgave / B. Zwart, A. Steenhuisen, m.m.v. H.J. Krijnen
184a Inleiding tot de algemene meteorologie : studie-uitgave ; 2e, druk / B. Zwart, A. Steenhuisen, m.m.v. H.J. Krijnen
185 Handleiding voor het gebruik van sectie 2 van de FM 13-X SHIP-code door stations op zee / KNMI; KLu; KM
185a Handleiding voor het gebruik van sectie 2 van de FM 13-X SHIP-code voor waarnemers op zee / KNMI; KLu; KM
186-I Rainfall generator for the Rhine Basin: single-site generation of weather variables by nearest-neighbour resampling / T. Brandsma and T.A. Buishand
187 De wind in de rug: KNMI-weerman schaatst de Elfstedentocht / Henk van Dorp

▼ TECHNISCH RAPPORT = TECHNICAL REPORT (TR)

168 Analyse van het seismische risico in Noord-Nederland / Th. de Crook, B. Dost en H.W. Haak
173 Measurement of the structure parameter of vertical wind-velocity in the atmospheric boundary layer / R. van der Ploeg
174 Report of the ASGASEX'94 workshop / ed. by W.A. Oost
175 Over slecht zicht, bewolking, windstoten en gladheid / J. Terpstra
176 Verification of the WAQUA/CSM-16 model for the winters 1992-93 and 1993-94 / J.W. de Vries
177 Nauwkeuriger nettostraling meten / M.K. van der Molen en W. Kohsiek
178 Neerslag in het stroomgebied van de Maas in januari 1995: waarnemingen en verificatie van modelprognoses / R.Jilderda ea.
179 First field experience with 600PA phased array sodar / H. Klein Baltink
180 Een Kalman-correctieschema voor de wegdektemperatuurverwachtingen van het VAISALA-model / A. Jacobs
181 Calibration study of the K-Gill propeller vane / Marcel Bottema
182 Ontwikkeling van een spectraal UV-meetinstrument / Frank Helderman
183 Rainfall generator for the Rhine catchment : a feasibility study / T. Adri Buishand and Theo Brandsma
184 Parametrisatie van mooi-weer cumulus / M.C. van Zanten
185 Interim report on the KNMI contributions to the second phase of the AERO-project / Wiel Wauben, Paul Fortuin ...[et al.]
186 Seismische analyse van de aardbevingen bij Middelstum (30 juli 1994) en Annen (16 augustus '94 en 31 januari '95) / [SO]
187 Analyse wenselijkheid overname RIVM-windmeetlokaties door KNMI / H. Benschop
188 Windsnelheidsmetingen op zeestations en kuststations: herleiding waarden windsnelheden naar 10-meter niveau / H. Benschop
189 On the KNMI calibration of net radiometers / W. Kohsiek
190 NEDWAM statistics over the period October 1994 - April 1995 / F.B. Koek
191 Description and verification of the HIRLAM trajectory model / E. de Bruijn
192 Tiltmeting : een alternatief voor waterpassing ? / H.W. Haak
193 Error modelling of scatterometer, in-situ and ECMWF model winds; a calibration refinement / Ad Stoffelen
194 KNMI contribution to the European project POPSICLE / Theo Brandsma and T. Adri Buishand
195 ECBILT : a coupled atmosphere ocean sea-ice model for climate predictability studies / R.J. Haarsma ao.
196 Environmental and climatic consequences of aviation: final report of the KNMI contributions to the AERO-project / W. Wauben ao.
197 Global radiation measurements in the operational KNMI meteorological network: effects of pollution and ventilation / F. Kuik
198 KALCORR: a kalman-correction model for real-time road surface temperature forecasting / A. Jacobs
199 Macroseismische waarnemingen Roswinkel 19-2-1997 / B. Dost en H.W Haak
200 Operationele UV-metingen bij het KNMI / F. Kuik
201 Vergelijking van de Vaisala's HMP233 en HMP243 relatieve luchtvochtigheidsmeters / F. Kuik
202 Statistical guidance for the North Sea / Janet Wijngaard and Kees Kok
203 UV-intercomparison SUSPEN / Foeke Kuik and Wiel Wauben
204 Temperature corrections on radiation measurements using Modtran 3 / D.A. Bunskoek, A.C.A.P. van Lammeren and A.J. Feijt
205 Seismisch risico in Noord-Nederland / Th. De Crook, H.W. Haak en B. Dost
206 The HIRLAM-STAT-archive and its application programs / Albert Jacobs

▼ WETENSCHAPPELIJK RAPPORT = SCIENTIFIC REPORT (WR)

95-01 Transformation of precipitation time series for climate change impact studies / A.M.G. Klein Tank and T.A. Buishand
95-02 Internal variability of the ocean generated by a stochastic forcing / M.H.B. van Noordenburg
95-03 Applicability of weakly nonlinear theory for the planetary-scale flow / E.A. Kartashova
95-04 Changes in tropospheric NOx and O3 due to subsonic aircraft emissions / W.M.F. Wauben ao.
95-05 Numerical studies on the Lorenz84 atmosphere model / L.Anastassiades
95-06 Regionalisation of meteorological parameters / W.C. de Rooy
95-07 Validation of the surface parametrization of HIRLAM using surface-based measurements and remote sensing data / A.F. Moene ao.
95-08 Probabilities of climatic change : a pilot study / Wieger Fransen (ed.) and Alice Reuvekamp
96-01 A new algorithm for total ozone retrieval from direct sun measurements with a filter instrument / W.M.F Wauben
96-02 Chaos and coupling: a coupled atmosphere ocean-boxmodel for coupled behaviour studies / G. Zondervan
96-03 An acoustical array for subsonic signals / H.W Haak
96-04 Transformation of wind in the coastal zone / V.N. Kudryavtsev and V.K. Makin
96-05 Simulations of the response of the ocean waves in the North Atlantic and North Sea to CO2 doubling in the atmosphere / K Rider ao.
96-06 Microbarograph systems for the infrasonic detection of nuclear explosions / H.W. Haak and G.J. de Wilde
96-07 An ozone climatology based on ozonesonde measurements / J.P.F. Fortuin
96-08 GOME validation at KNMI and collaborating institutes / ed. by P Stammes and A. Piters
97-01 The adjoint of the WAM model / H. Hersbach
97-02 Optimal interpolation of partitions: a data assimilation scheme for NEDWAM-4; description and evaluation of the period November 1995 - October 1996 / A.Voorrips
97-03 SATVIEW: a semi-physical scatterometer algorithm / J.A.M. Janssen and H. Wallbrink
97-04 GPS water vapour meteorology : status report / H. Derks, H. Klein Baltink, A. van Lammeren, B. Ambrosius, H. van der Marel ao.
97-05 Climatological spinup of the ECBILT oceanmodel / Arie Kattenberg and Sybren S. Drijfhout
97-06 Direct determination of the air-sea transfer velocity of CO2 during ASGAMAGE / J.C.M. Jacobs, W. Kohsiek and W.A. Oost
97-07 Scattering matrices of ice crystals / M. Hess, P. Stammes and R.B.A. Koelemeijer
97-08 Experiments with horizontal diffusion and advection in a nested fine mesh mesoscale model / E.I.F. de Bruijn
97-09 On the assimilation of ozone into an atmospheric model / E.Valur Hólm
98-01 Steady state analysis of a coupled atmosphere ocean-boxmodel / F.A. Bakker
98-02 The ASGAMAGE workshop, September 22-25, 1997 / ed. W.A. Oost
98-03 Experimenting with a similarity measure for atmospheric flows / R.A. Pasmanter and X.-L. Wang
98-04 Evaluation of a radio interferometry lightning positioning system / H.R.A. Wessels